

## Article

# Divalent Europium, NIR and Variable Emission of Trivalent Tm, Ho, Pr, Er, Nd, and Ce in 3D Frameworks and 2D Networks of Ln–Pyridylpyrazolates

 Heba Youssef <sup>1,2</sup> , Jonathan Becker <sup>1</sup> , Clemens Pietzonka <sup>3</sup>, Ilya V. Taydakov <sup>4,5</sup> , Florian Kraus <sup>3</sup>   
 and Klaus Müller-Buschbaum <sup>1,6,\*</sup>

- <sup>1</sup> Institute of Inorganic and Analytical Chemistry, Justus-Liebig-University Giessen, Heinrich-Buff-Ring 17, 35392 Giessen, Germany; heba.youssef@anorg.chemie.uni-giessen.de (H.Y.)
- <sup>2</sup> Department of Chemistry, Faculty of Science, Mansoura University, El Gomhouria, Mansoura Qism 2, Dakahlia Governorate, Mansoura 11432, Egypt
- <sup>3</sup> Fachbereich Chemie, Philipps-University Marburg, Hans-Meerwein-Straße, 35032 Marburg, Germany
- <sup>4</sup> Lebedev Physical Institute of the Russian Academy of Sciences, Leninskiy pr-t, 53, 119991 Moscow, Russia
- <sup>5</sup> Basic Department of Chemistry of Innovative Materials and Technologies, G.V. Plekhanov Russian University of Economics, Stremyanny Per. 36, 117997 Moscow, Russia
- <sup>6</sup> Center of Materials Research (LAMA), Justus-Liebig-University Giessen, Heinrich-Buff-Ring 16, 35392 Giessen, Germany
- \* Correspondence: klaus.mueller-buschbaum@anorg.chemie.uni-giessen.de

**Abstract:** The redox reactions of various lanthanide metals with 3-(4-pyridyl)pyrazole (4-PyPzH) or 3-(3-pyridyl)pyrazole (3-PyPzH) ligands yield the 2D network  ${}^2_{\infty}[\text{Eu}(4\text{-PyPz})_2(\text{Py})_2]$  containing divalent europium, the 3D frameworks  ${}^3_{\infty}[\text{Ln}(4\text{-PyPz})_3]$  and  ${}^3_{\infty}[\text{Ln}(3\text{-PyPz})_3]$  for trivalent cerium, praseodymium, neodymium, holmium, erbium, and thulium as well as  ${}^3_{\infty}[\text{La}(4\text{-PyPz})_3]$ , and the 2D networks  ${}^2_{\infty}[\text{Ln}(4\text{-PyPz})_3(\text{Py})]$  for trivalent cerium and thulium and  ${}^2_{\infty}[\text{Ln}_2(4\text{-PyPz})_6]\cdot\text{Py}$  for trivalent ytterbium and lutetium. The 18 lanthanide coordination polymers were synthesized under solvothermal conditions in pyridine (Py), partly acting as a co-ligand for some networks. The compounds exhibit a variety of luminescence properties, including metal-centered 4f–4f/5d–4f emission in the visible and near-infrared spectral range, metal-to-ligand energy transfer, and ligand-centered fluorescence and phosphorescence. The anionic ligands 3-PyPz<sup>−</sup> and 4-PyPz<sup>−</sup> serve as suitable antennas for lanthanide-based luminescence in the visible and near-infrared range through effective sensitization followed by emission through intra-4f transitions of the trivalent thulium, holmium, praseodymium, erbium, and neodymium.  ${}^2_{\infty}[\text{Ce}(4\text{-PyPz})_3(\text{Py})]$ ,  ${}^3_{\infty}[\text{Ce}(4\text{-PyPz})_3]$ , and  ${}^3_{\infty}[\text{Ce}(3\text{-PyPz})_3]$  exhibit strong degrees of reduction in the 5d excited states that differ in intensity compared to the ligand-based emission, resulting in a distinct emission ranging from pink to orange. The direct current magnetic studies show magnetic isolation of the lanthanide centers in the crystal lattice of  ${}^3_{\infty}[\text{Ln}(3\text{-PyPz})_3]$ , Ln = Dy, Ho, and Er.

**Keywords:** divalent europium; cerium; NIR emitter; N-donor ligand



**Citation:** Youssef, H.; Becker, J.; Pietzonka, C.; Taydakov, I.V.; Kraus, F.; Müller-Buschbaum, K. Divalent Europium, NIR and Variable Emission of Trivalent Tm, Ho, Pr, Er, Nd, and Ce in 3D Frameworks and 2D Networks of Ln–Pyridylpyrazolates. *Chemistry* **2023**, *5*, 1006–1027. <https://doi.org/10.3390/chemistry5020069>

Academic Editors: Christoph Janiak, Sascha Rohn and Georg Manolikakes

Received: 27 March 2023

Revised: 20 April 2023

Accepted: 26 April 2023

Published: 28 April 2023



**Copyright:** © 2023 by the authors. Licensee MDPI, Basel, Switzerland. This article is an open access article distributed under the terms and conditions of the Creative Commons Attribution (CC BY) license (<https://creativecommons.org/licenses/by/4.0/>).

## 1. Introduction

Divalent europium, the mildest reducing agent of the redox-sensitive divalent lanthanide ions, has been successfully used in a wide variety of material applications such as medical imaging [1,2], photochemistry [3,4], lanthanide-activated phosphors [5,6], and sensing [7,8]. Trivalent lanthanides are known for their luminescence properties, with f–f based emission covering the spectrum from the ultraviolet (UV) to the near-infrared (NIR) spectral region, characteristic for each metal ion [9,10]. Several ions of typical NIR emitters also have possible transitions in the visible range [11], but these are usually too weak to be readily observed, especially for Tm<sup>3+</sup> and Ho<sup>3+</sup> [12–16]. NIR emitters have played an important role in many modern technologies such as organic light-emitting

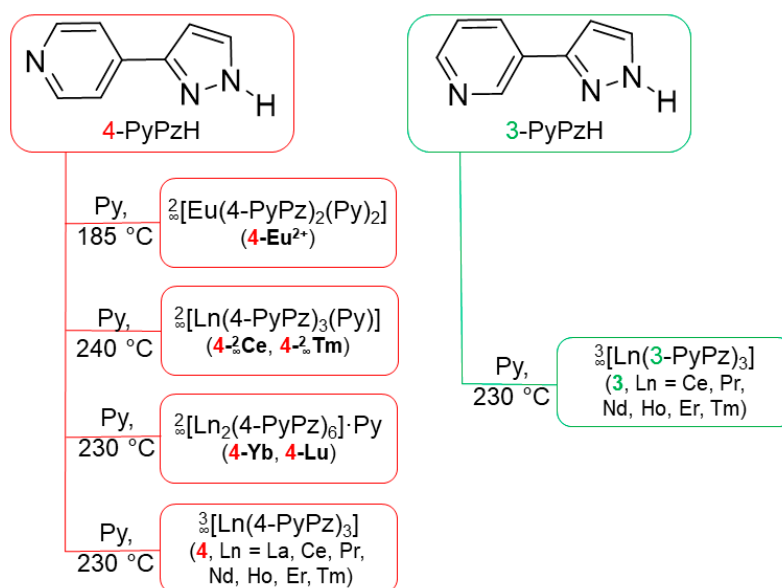
diodes (OLEDs) [17,18] and photovoltaics [19,20], which encouraged us to further study the photophysical properties of NIR emitters such as Tm, Ho, Nd, and Er [11,12,21,22].

In addition to the forbidden f–f transitions, 5d–4f transitions can also be detected among the trivalent and the divalent lanthanides such as  $\text{Ce}^{3+}$  and  $\text{Eu}^{2+}$ . The 5d–4f transitions have also been studied for decades on the luminescent mechanism and potential applications in various fields [23–25]. The emission occurs in the UV and/or in the blue spectral regions but can be shifted to a much longer wavelength depending on the environment of the  $\text{Ln}^{3+}$  ion [26,27]. Mostly, the 5d–4f transitions are absent due to thermal quenching by fast intersystem crossing from  $4f^{n-1}5d^1$  to  $4f^n$  configuration [4,28]. Pink-emitting cerium has rarely been detected in doped materials such as cerium-doped single-crystal aluminum nitride [29] and cerium–manganese-activated phosphor [30] and not for undoped systems. Furthermore, undoped red-emitting  ${}^1_{\infty}[\text{Ce}(2\text{-PyPz})_3]$  and orange-emitting  $[\text{Ce}(2\text{-PyPzH})_3\text{Cl}_3]$  (2-PyPzH = 3-(2-pyridyl)pyrazole) were just recently reported for orange emission [31,32]. These results inspired further investigations on the influence of changing the position of the nitrogen of the pyridyl ring in 3-(4-pyridyl)pyrazole (4-PyPzH) and 3-(3-pyridyl)pyrazole (3-PyPzH), which are presented in this work. The ligands 4-PyPzH and 3-PyPzH were used to synthesize homoleptic and highly luminescent trivalent lanthanide 3D coordination polymers with the formulas  ${}^3_{\infty}[\text{Ln}(3\text{-PyPz})_3]$  and  ${}^3_{\infty}[\text{Ln}(4\text{-PyPz})_3]$ , Ln = Sm, Eu, Gd, Tb, Dy [33]. Neither 3-PyPzH nor 4-PyPzH as ligands have been explored for complexing divalent lanthanide ions. Following the reaction of europium metal with 4-PyPzH, a 2D network based on divalent europium was synthesized and presented in this work.

3-PyPzH was used to synthesize a wide variety of structures, from 3D and 2D networks to complexes of lanthanide trichlorides [14]. The weak ferromagnetic interaction for  ${}^2_{\infty}[\text{Ho}_2(3\text{-PyPzH})_3\text{Cl}_6] \cdot 2\text{MeCN}$  encouraged us to study the magnetic properties of the presented Ln metal-based series.

## 2. Results and Discussion

Elemental lanthanides together with 3-(4-pyridyl)pyrazole (4-PyPzH) or 3-(3-pyridyl)pyrazole (3-PyPzH) in solvothermal synthesis-based reactions were used to obtain eighteen 3D frameworks and 2D networks (Scheme 1).



**Scheme 1.** Synthetic scheme for reactions of lanthanide metals with 4-PyPzH and 3-PyPzH to obtain 3D frameworks and 2D networks.

### 2.1. Structural Analysis

Structural diversity is observed along the series based on 4-PyPz<sup>−</sup>, depending on the content of both 4-PyPz<sup>−</sup> and pyridine (Py) as linkers, all of which crystallize in the monoclinic crystal system and mostly with the space group  $P2_1/n$ . Exceptions are  ${}^2_{\infty}[\text{Eu}(4\text{-PyPz})_2(\text{Py})_2]$  (**4-Eu<sup>2+</sup>**) and  ${}^2_{\infty}[\text{Ln}(4\text{-PyPz})_3(\text{Py})]$ , Ln = Ce (**4-<sup>2</sup>Ce**), Tm (**4-<sup>2</sup>Tm**), which crystallize with the space groups  $P2_1$  and  $Cc$ , respectively. The other 3-PyPz<sup>−</sup> based series  ${}^3_{\infty}[\text{Ln}(3\text{-PyPz})_3]$ , (**3**, Ln = Ce, Pr, Nd, Ho, Er, Tm) further crystallizes in the cubic crystal system with the space group  $Pa\bar{3}$ .

In  ${}^2_{\infty}[\text{Eu}(4\text{-PyPz})_2(\text{Py})_2]$  (**4-Eu<sup>2+</sup>**), containing divalent europium, each Eu<sup>2+</sup> ion coordinates to eight nitrogen atoms, six nitrogen atoms from four pyrazolate anions, and two nitrogen atoms from two pyridine molecules in a distorted pseudo-octahedral assembly (Figure 1), if the two nitrogen atoms of the pyrazolate anion are considered as one corner of the octahedron. The four pyrazolate anions act as bridges to the neighboring Eu<sup>2+</sup> ions, forming a 2D coordination polymer. The Eu–N interatomic distances for divalent europium in  ${}^2_{\infty}[\text{Eu}(4\text{-PyPz})_2(\text{Py})_2]$  (**4-Eu<sup>2+</sup>**) (254.9(4)–274.5(2) pm) are longer than those reported for the trivalent europium  ${}^3_{\infty}[\text{Eu}(4\text{-PyPz})_3]$  (240.8–258.8 pm) [33], consistent with the difference in charge density and ionic radius [34]. Another comparison of the Eu–N of **4-Eu<sup>2+</sup>** with the divalent europium complex  $[\text{Eu}(\text{Ph}_2\text{pz})_2(\text{Py})_4] \cdot 2\text{Py}$  (Ph<sub>2</sub>pz = 3,5-diphenylpyrazolate, Eu–N = 253.8–274.1 pm) resulted in good agreement [35].

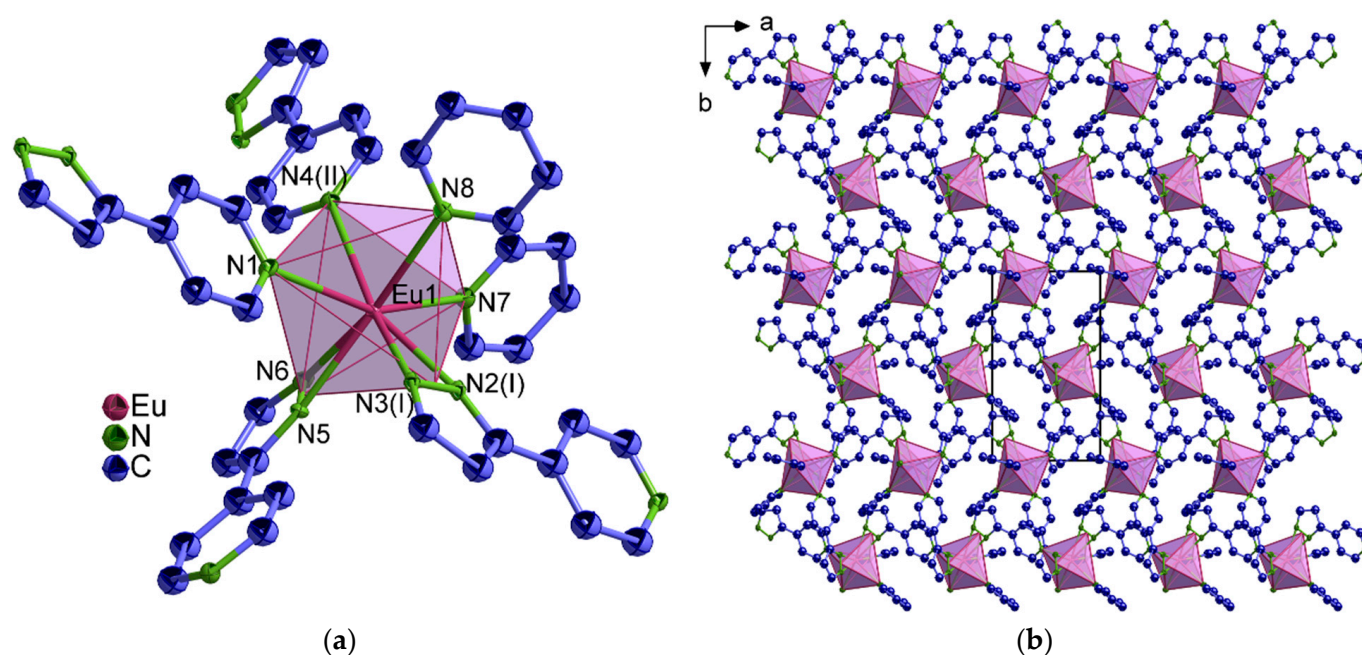


**Figure 1.** (a) Extended coordination sphere of the Eu<sup>2+</sup> ion in  ${}^2_{\infty}[\text{Eu}(4\text{-PyPz})_2(\text{Py})_2]$  (**4-Eu<sup>2+</sup>**); (b) crystal structure of **4-Eu<sup>2+</sup>** with a view along [001]. The coordination polyhedra around Eu<sup>2+</sup> are indicated in violet with thermal ellipsoids depicted at the 50% probability level. Symmetry operations: I  $x + 1, y, z$  II  $-x + 1, y + 1/2, -z$ . In all figures, the hydrogen atoms are omitted for clarity and the unit cell is depicted when required.

In  ${}^2_{\infty}[\text{Ln}(4\text{-PyPz})_3(\text{Py})]$ , Ln = Ce<sup>3+</sup> (**4-<sup>2</sup>Ce**), Tm<sup>3+</sup> (**4-<sup>2</sup>Tm**), each Ln<sup>3+</sup> ion coordinates to nine nitrogen atoms, eight nitrogen atoms from five pyrazolate anions, and a nitrogen atom from a pyridine molecule in a distorted pseudo-octahedral arrangement (Figure 2), if the two nitrogen atoms of the pyrazolate anion are viewed as one corner of the octahedron. The pyrazolate anions act as bridges to the neighboring Ln<sup>3+</sup> ions, forming a 2D coordination polymer. Due to the lack of Tm<sup>3+</sup>-nitrogen-based complexes and coordination polymers in the literature, only one example was comparable to **4-<sup>2</sup>Tm**,  $[\text{Tm}(\text{L}^1)_3]^{3+}$  (L<sup>1</sup> = 2,6-bis(5,6-dipropyl-1,2,4-triazin-3-yl)pyridine, Tm–N = 248.3–252.2 pm) [36], which is longer than **4-<sup>2</sup>Tm** (Tm–N = 232.4–259.2 pm) due to the anionic character of the ligands, in the latter 4-PyPz<sup>−</sup>.

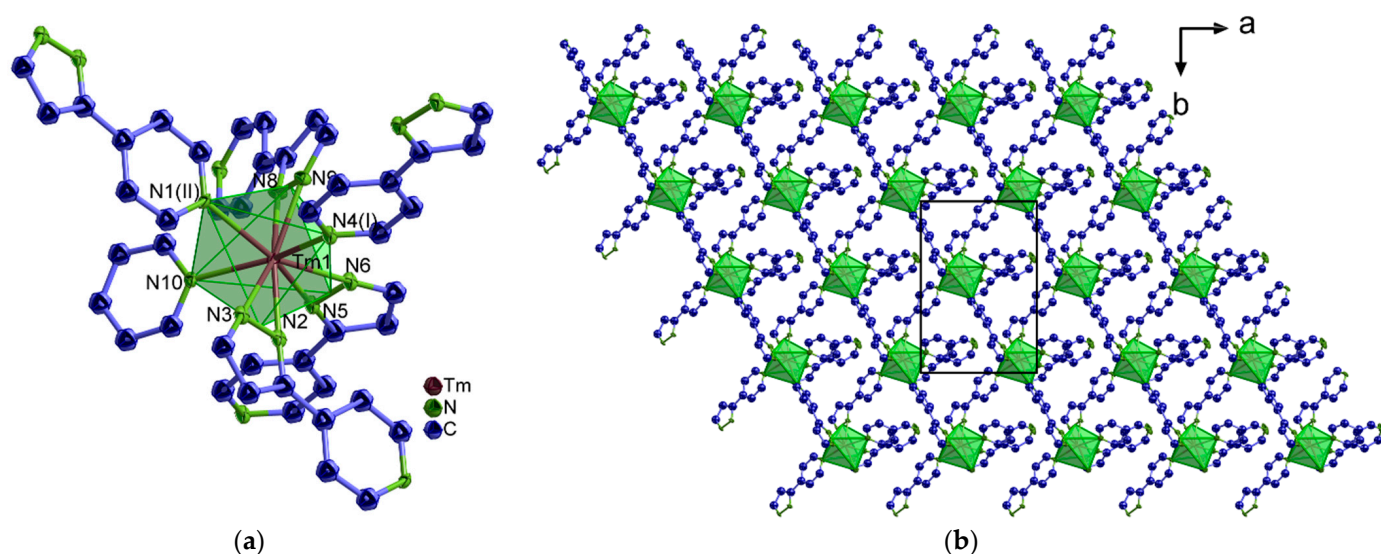


**Figure 2.** (a) Extended coordination sphere of  $\text{Tm}^{3+}$  in  ${}^2_{\infty}[\text{Tm}(\text{4-PyPz})_3(\text{Py})]$  ( $4-{}^2_{\infty}\text{Tm}$ ); (b) crystal structure of  $4-{}^2_{\infty}\text{Tm}$  with a view along  $[001]$ . The coordination polyhedra around  $\text{Tm}^{3+}$  are indicated in green with thermal ellipsoids depicted at the 50% probability level. Symmetry operations:  $I x - 1/2, y + 1/2, z \parallel x + 1/2, y + 1/2, z$ .

The topology of the  $4\text{-Eu}^{2+}$  and  $4-{}^2_{\infty}\text{Tm}$  networks was determined according to the Reticular Chemistry Structure Resource (RCSR) and the Wells terminology [37,38] to result in an **sql** topology (Figure 3) with the Schläfli symbol  $4^4 \cdot 6^2$  for both cases. This topology distinguishes from the rest of the series  ${}^3_{\infty}[\text{Ln}(\text{4-PyPz})_3]$  ( $4$ , Ln = La, Ce, Pr, Nd, Ho, Er, Tm), which represent the **pcu** topology with the Schläfli symbol  $4^{12} \cdot 6^3$  [33]. The **pcu** topology was also found for the isotopic series  ${}^3_{\infty}[\text{Ln}(\text{3-PyPz})_3]$  ( $3$ , Ln = Ce, Pr, Nd, Ho, Er, Tm).

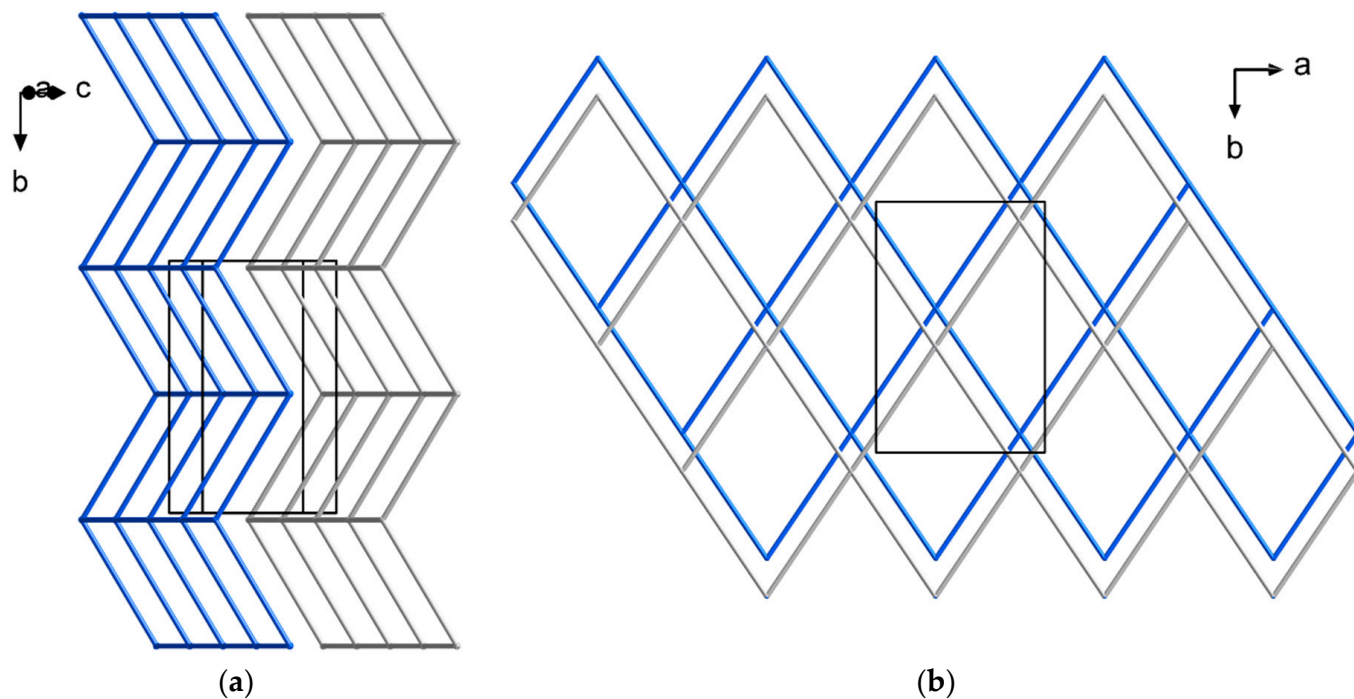


**Figure 3.** Topological representation of (a)  ${}^2_{\infty}[\text{Eu}(\text{4-PyPz})_2(\text{Py})_2]$  ( $4\text{-Eu}^{2+}$ ); (b)  ${}^2_{\infty}[\text{Tm}(\text{4-PyPz})_3(\text{Py})]$  ( $4-{}^2_{\infty}\text{Tm}$ ) as a uninodal 4-c net with **sql** topology.

The crystal structure of  ${}^2_{\infty}[\text{Ln}_2(\text{4-PyPz})_6]\text{Py}$ , Ln = Yb ( $4\text{-Yb}$ ), Lu ( $4\text{-Lu}$ ) contains two lanthanide sites. One site coordinates to nine nitrogen atoms from six pyrazolate anions in a

distorted pseudo-octahedron, while the other coordinates to eight nitrogen atoms from five pyrazolate anions in a distorted trigonal bipyramid (Figure 4), if the two nitrogens of the pyrazolate anion are considered as a corner of the polyhedron. The two lanthanide sites are bridged through a pyrazolate anion, while each lanthanide site is simultaneously bridged through pyrazolate anions to adjacent identical sites to form a 2D layer extending along the *bc* plane. An anion coordinated to Ln1 does not act as a bridge through the nitrogen atom of its pyridine ring to another neighboring Ln ion (its position is pointed by arrows in Figure 4), making some ligands infinite and, thus, a correct topological analysis with the central atoms impossible.

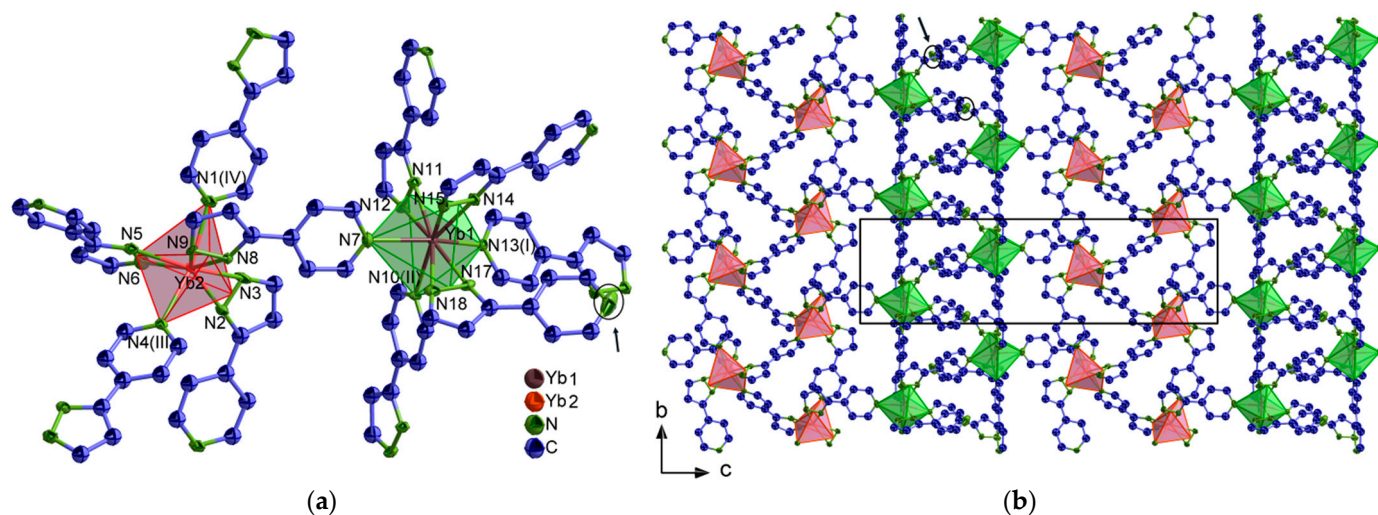


**Figure 4.** (a) Extended coordination sphere of  $\text{Yb}^{3+}$  in  ${}_{\infty}^2[\text{Yb}_2(4\text{-PyPz})_6]$  (**4-Yb**); (b) crystal structure of **4-Yb** with a view along [100]. The coordination polyhedra around Yb1 and Yb2 are indicated in green and red, respectively. The arrows point to the uncoordinated nitrogen atom. The solvent molecules are omitted for clarity. Symmetry operations: I  $-x + 1/2, y - 1/2, -z + 1/2$  II  $x, y - 1, z$  III  $-x + 1/2, y - 1/2, -z + 3/2$  IV  $x, y + 1, z$ .

The different coordination numbers are also reflected by the Yb–N distances, which range from 227.7(6)–247.9(6) pm for CN = 8 (Yb2) to 234.1(6)–257.5(5) pm for CN = 9 (Yb1). Comparison of the Yb–N distances with  $[\text{Yb}(\text{Ph}_2\text{pz})_3(\text{Py})_2] \cdot 2(\text{thf})$  ( $\text{Ph}_2\text{pz}$  = 3,5-diphenylpyrazolate, CN = 8, Yb–N = 225.7–244.3 pm) [39] and  $[\text{YbL}_3] \cdot \text{CH}_3\text{OH}$  (HL = 2-(tetrazol-5-yl)-1,10-phenanthroline, CN = 9, Yb–N = 240.9–259.9) [40] shows good agreement for Yb–N. The Yb2–N<sub>pz</sub> (pz = pyrazolate nitrogen atom) is slightly shorter than the reported range, indicating the strength of the electrostatic interaction between the metal cation and the anionic pyrazolate ring.

The crystal structures of  ${}_{\infty}^3[\text{Ln}(4\text{-PyPz})_3]$  (**4**, Ln = La, Ce, Pr, Nd, Ho, Er, Tm) and  ${}_{\infty}^3[\text{Ln}(3\text{-PyPz})_3]$  (**3**, Ln = Ce, Pr, Nd, Ho, Er, Tm) are isotypic to the respective reported series of  ${}_{\infty}^3[\text{Ln}(4\text{-PyPz})_3]$  and  ${}_{\infty}^3[\text{Ln}(3\text{-PyPz})_3]$ , Ln = Sm, Eu, Gd, Tb, Dy, respectively [33]. The extended coordination sphere of  $\text{Ce}^{3+}$  (CN = 9) in the two isotypic series  ${}_{\infty}^3[\text{Ln}(4\text{-PyPz})_3]$  and  ${}_{\infty}^3[\text{Ln}(3\text{-PyPz})_3]$  are shown in Figures S1 and S2. The volume of the unit cell and the average of Ln–N decrease with the increasing charge density along the two series  ${}_{\infty}^3[\text{Ln}(4\text{-PyPz})_3]$  and  ${}_{\infty}^3[\text{Ln}(4\text{-PyPz})_3]$  (Tables S10 and S11) as a direct consequence of the lanthanide contraction [41]. Tables with detailed crystallographic data and selected interatomic distances (pm) and angles ( $^\circ$ ) of the studied compounds are given in the Supplementary Materials (Tables S1–S11).

The crystal structures were mostly determined by single-crystal X-ray diffraction (SCXRD), while the structures of  ${}_{\infty}^2[\text{Ce}(4\text{-PyPz})_3(\text{Py})]$  (**4- $\infty^2$  Ce**) and  ${}_{\infty}^3[\text{Tm}(4\text{-PyPz})_3]$  (**4-Tm**) were characterized from microcrystalline products by powder X-ray diffraction (PXRD) and subsequent Pawley refinements (Figure 5a,b), confirming the isotypic character based on the SCXRD of  ${}_{\infty}^2[\text{Tm}(4\text{-PyPz})_3(\text{Py})]$  (**4- $\infty^2$  Tm**) and  ${}_{\infty}^3[\text{Er}(4\text{-PyPz})_3]$  (**4-Er**), respectively.

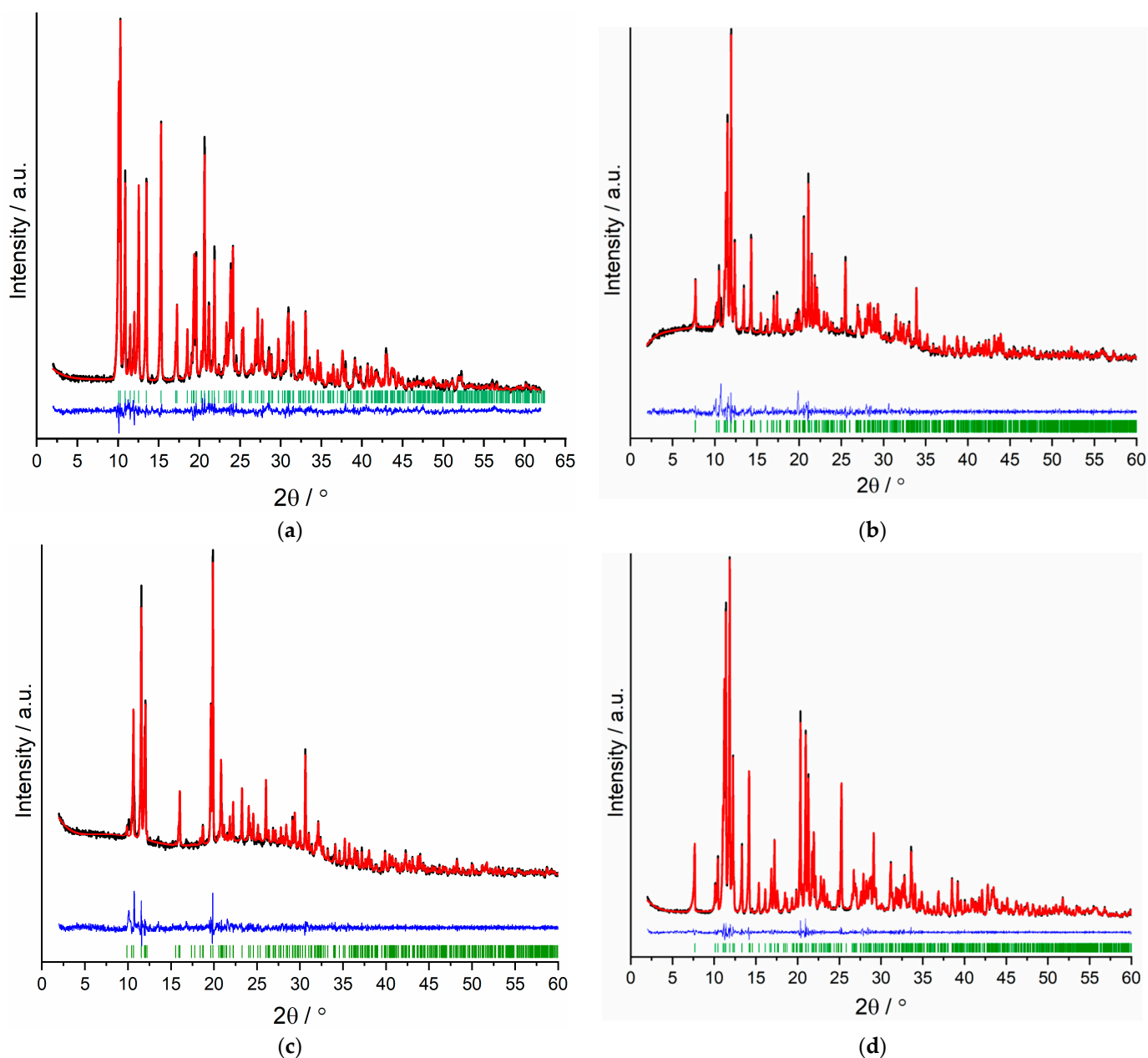


**Figure 5.** Pawley refinement results for PXR D of (a)  ${}^2_{\infty}[\text{Ce}(4\text{-PyPz})_3(\text{Py})]$  (**4- ${}^2_{\infty}\text{Ce}$** ), (b)  ${}^3_{\infty}[\text{Tm}(4\text{-PyPz})_3]$  (**4- ${}^3_{\infty}\text{Tm}$** ), (c)  ${}^2_{\infty}[\text{Eu}(4\text{-PyPz})_2(\text{Py})_2]$  (**4- $\text{Eu}^{2+}$** ), and (d)  ${}^3_{\infty}[\text{Ce}(4\text{-PyPz})_3]$  (**4- ${}^3_{\infty}\text{Ce}$** ), showing the experimental data (black) together with the Pawley fit (red), the corresponding difference plot (blue), as well as hkl position markers (green).

All bulk products were investigated by PXR D. For  ${}^3_{\infty}[\text{Ln}(3\text{-PyPz})_3]$  (**3**, Ln = Ce, Pr, Nd, Ho, Er), the experimental diffraction patterns agree with the diffraction patterns simulated from the single-crystal data with no observation of additional reflections indicating the absence of crystalline byproducts (Figure S3). To account for the different measurement conditions of PXR D (298 K) and SCXR D (100 K), Pawley refinements for  ${}^2_{\infty}[\text{Eu}(4\text{-PyPz})_2(\text{Py})_2]$  (**4- $\text{Eu}^{2+}$** ) (Figure 5c),  ${}^3_{\infty}[\text{Ce}(4\text{-PyPz})_3]$  (**4- ${}^3_{\infty}\text{Ce}$** ) (Figure 5d), and  ${}^3_{\infty}[\text{Ln}(4\text{-PyPz})_3]$  (**4**, Ln = La, Pr, Nd, Ho, Er) (Figures S4–S8) were carried out, confirming the phase purity of the respective series of coordination polymers. The resulting difference plots show no significant deviations, and the refinement results ( $R_{\text{wp}}$ , GOF) are shown in Table S12. Other crystalline phases were found in the PXR D of  ${}^2_{\infty}[\text{Tm}(4\text{-PyPz})_3(\text{Py})]$  (**4- ${}^2_{\infty}\text{Tm}$** ) and  ${}^2_{\infty}[\text{Ln}_2(4\text{-PyPzH})_6]\text{Py}$ ,

Ln = Yb (**4-Yb**), Lu (**4-Lu**) (Figure S9). Isolation of  ${}^3\infty[\text{Tm}(\text{3-PyPz})_3]$  (**3-Tm**) as single crystals was also possible.

## 2.2. Photophysical Properties

### 2.2.1. UV–VIS–NIR Absorption Spectra

Electronic absorption spectra were recorded in the solid state at room temperature (RT) for 4-PyPzH,  ${}^2\infty[\text{Eu}(\text{4-PyPz})_2(\text{Py})_2]$  (**4-Eu<sup>2+</sup>**),  ${}^2\infty[\text{Ce}(\text{4-PyPz})_3(\text{Py})]$  (**4-<sup>2</sup>Ce**),  ${}^3\infty[\text{Ln}(\text{4-PyPz})_3]$  (**4**, Ln = Ce, Pr, Nd, Ho, Er, Tm), and  ${}^3\infty[\text{Ln}(\text{3-PyPz})_3]$  (**3**, Ln = Ce, Pr, Nd, Ho, Er) (Figure 6). The absorption spectra of the free ligand 3-PyPzH was shown for the solid state in a range from about 200–270 and 570–305 nm corresponding to the intra-ligand transitions  $\pi-\pi^*$  and/or  $n-\pi^*$  [14]. The free ligand 4-PyPzH shows a broad band from 200 to 280 nm corresponding to the intra-ligand transitions. In the investigated coordination polymers, the intense wide absorption band corresponding to either ligand appears in the UV region. For  ${}^2\infty[\text{Eu}(\text{4-PyPz})_2(\text{Py})_2]$  (**4-Eu<sup>2+</sup>**), a broad absorption shoulder from 356–640 nm is associated with a metal-to-ligand charge transfer (MLCT) transition from the  $\text{Eu}^{2+}$  4f orbitals to the  $\pi^*$  orbitals of the coordinated ligands. For  ${}^2\infty[\text{Ce}(\text{4-PyPz})_3(\text{Py})]$  (**4-<sup>2</sup>Ce**),  ${}^3\infty[\text{Ce}(\text{4-PyPz})_3]$  (**4-Ce**), and  ${}^3\infty[\text{Ce}(\text{3-PyPz})_3]$  (**3-Ce**), the formation of shoulders at a higher wavelength from 320–470 nm is observed due to the transition from 4f to 5d. These absorption shoulders are compatible with the shoulders observed for the orange and the red emitters  $[\text{Ce}(\text{2-PyPzH})_3\text{Cl}_3]$  and  ${}^1\infty[\text{Ce}(\text{2-PyPz})_3]$  [31]. Moreover, sharp and weak to medium bands can be assigned to the respective f–f transitions in both the VIS and NIR regions for  ${}^3\infty[\text{Ln}(\text{4-PyPz})_3]$ , Ln = Pr (**4-Pr**), Nd (**4-Nd**), Ho (**4-Ho**), Er (**4-Er**), Tm (**4-Tm**) and  ${}^3\infty[\text{Ln}(\text{3-PyPz})_3]$ , Ln = Pr (**3-Pr**), Nd (**3-Nd**), Ho (**3-Ho**), Er (**3-Er**), as assigned in Table 1 [11,42–45].

### 2.2.2. Emission and Excitation Spectra

The photoluminescence properties were recorded for all bulk products,  ${}^2\infty[\text{Eu}(\text{4-PyPz})_2(\text{Py})_2]$  (**4-Eu<sup>2+</sup>**),  ${}^2\infty[\text{Ce}(\text{4-PyPz})_3(\text{Py})]$  (**4-<sup>2</sup>Ce**),  ${}^3\infty[\text{Ln}(\text{4-PyPz})_3]$  (**4**, Ln = La, Ce, Pr, Nd, Ho, Er, Tm), and  ${}^3\infty[\text{Ln}(\text{3-PyPz})_3]$  (**3**, Ln = Ce, Pr, Nd, Ho, Er) in the solid state at RT and 77 K. The photoluminescence spectroscopy determinations for  ${}^2\infty[\text{Ce}(\text{4-PyPz})_3(\text{Py})]$  (**4-<sup>2</sup>Ce**),  ${}^3\infty[\text{Ce}(\text{4-PyPz})_3]$  (**4-Ce**), and  ${}^3\infty[\text{Ce}(\text{3-PyPz})_3]$  (**3-Ce**) (Figure 7) show interesting 5d–4f transitions with  $\text{Ce}^{3+}$ -centered light emission in the VIS range. Broad emission bands appear for **4-<sup>2</sup>Ce**, **4-Ce**, and **3-Ce** from 520, 500, and 460 to 850 nm centered at 650, 650, and 641 nm, respectively, at RT, indicating large crystal field splitting and a large redshift for the emission wavelength reaches the red–orange visible region. The intensity of the ligand-based emission decreases from **4-<sup>2</sup>Ce** through **4-Ce** to **3-Ce** which shifts the emission color from pink through orange pink to orange, the emission colors are represented in the CIE 1931 chromaticity diagram (Figure S24), and the color coordinates are listed in Table S13. In agreement with the absorption spectra, the excitation spectra show shoulders at higher wavelengths, which correlate with the lowest energy levels of the crystal field splitting bands of the 5d excited state of the  $\text{Ce}^{3+}$  ions.

The maximum excitation bands are at about 400 nm, corresponding to the respective coordinated pyrazolate anions. The lifetimes of **4-<sup>2</sup>Ce** (1.08(2) ns), **4-Ce** (1.16(2) ns), and **3-Ce** (1.26(2) ns) are expected to be nanoseconds due to the parity allowed nature of the 5d–4f transition. These lifetimes are slightly shorter than the lifetimes of the reported red-emitting cerium  ${}^1\infty[\text{Ln}(\text{2-PyPz})_3]$  (2 ns, 2-PyPzH = 3-(2-pyridyl)pyrazole) [32] and orange-emitting cerium  $[\text{Ce}(\text{2-PyPzH})_3\text{Cl}_3]$  (2.83 ns) [31].

The emission spectrum of  ${}^2\infty[\text{Eu}(\text{4-PyPz})_2(\text{Py})_2]$  (**4-Eu<sup>2+</sup>**) shows a ligand-based transition at 350 nm (Figure 7) along with some weak f–f transitions that can be assigned to a low content of trivalent Eu emission features. The ligand-based excitation band at around 335 nm for 4-PyPzH and 3-PyPzH [33] shows a hypochromic shift upon coordination to the investigated compounds to around 325 nm in **4-Pr**, **4-Nd**, **3-Nd**, **3-Ho**, **4-Er**, **3-Er**, and **4-Tm**. The blue shift for the ligand-based excitation band increases, reaching 318 nm for **3-Pr** and **4-Ho** and even below 300 nm for **4-Eu<sup>2+</sup>**. For  $\text{Pr}^{3+}$ ,  $\text{Nd}^{3+}$ , and  $\text{Er}^{3+}$ , additional direct f–f excitations from the ground states  ${}^3\text{H}_4$ ,  ${}^4\text{I}_{9/2}$ , and  ${}^4\text{I}_{15/2}$ , respectively, were also observed.

After coordination, the ligand-based emission band for both ligands at 405 nm shows a hypochromic shift to a value between 341 and 352 nm.

For  ${}^3[\text{Ln}(\text{4-PyPz})_3]$  (**4-Ln**), an additional resolved broad band with  $\lambda_{\text{onset}} = 423$  nm ( $\sim 23,640$   $\text{cm}^{-1}$ ), corresponding to the triplet state of the pyrazolate anion, was observed in the emission spectrum (Figure S27) at 77 K, which agrees well with the previously reported value [33].

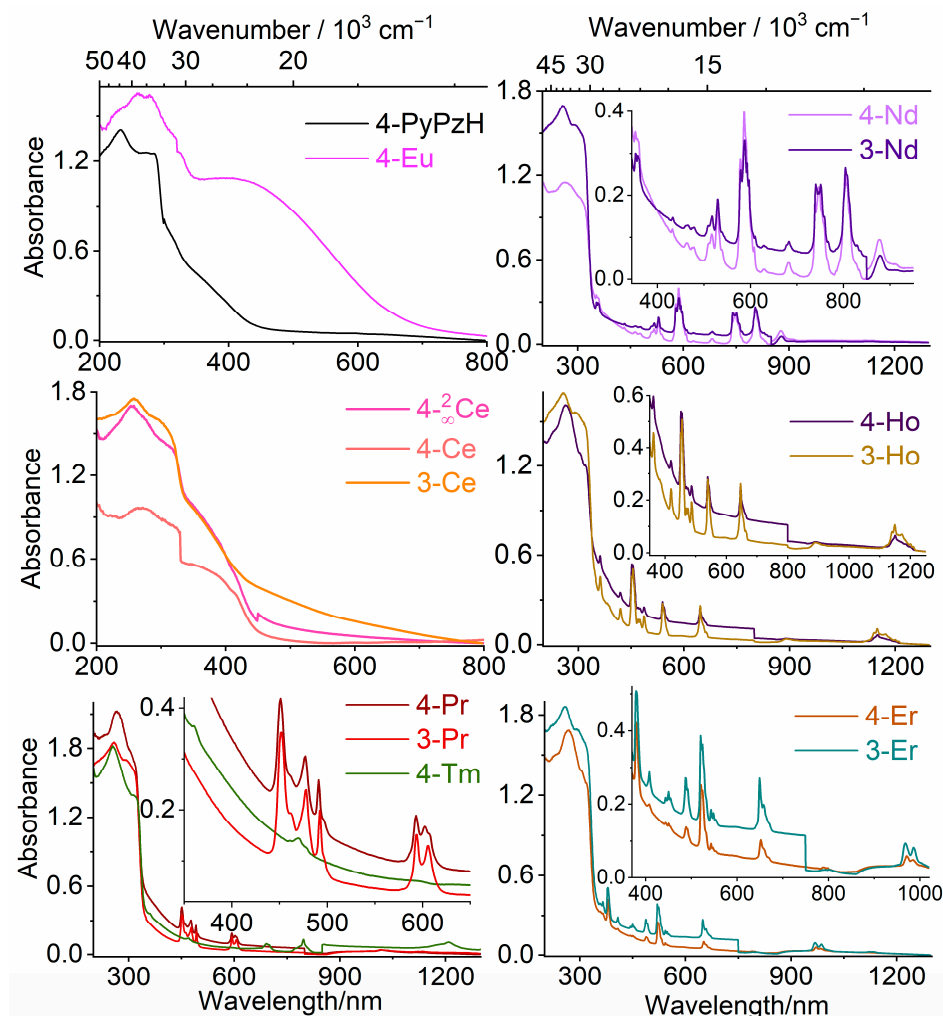


**Figure 6.** Solid-state absorption spectra of 4-PyPzH,  ${}^2[\text{Eu}(\text{4-PyPz})_2(\text{Py})_2]$  (**4-Eu<sup>2+</sup>**),  ${}^2[\text{Ce}(\text{4-PyPz})_3(\text{Py})]$  (**4-<sup>2</sup>Ce**),  ${}^3[\text{Ln}(\text{4-PyPz})_3]$ , (**4, Ln = Ce, Pr, Nd, Ho, Er, Tm**) and  ${}^3[\text{Ln}(\text{3-PyPz})_3]$ , (**3, Ln = Ce, Pr, Nd, Ho, Er**) in the solid state at room temperature.

**Table 1.** Absorption wavelengths of transitions of  ${}^3[\text{Ln}(\text{4-PyPz})_3]$ , (**4, Ln = Pr, Nd, Ho, Er, Tm**) and  ${}^3[\text{Ln}(\text{3-PyPz})_3]$ , (**3, Ln = Pr, Nd, Ho, Er**) in the solid state at room temperature.

| ID           | Intra-4f Absorption Transitions   |   | $\lambda_{\text{max}}$ (nm)                     |
|--------------|-----------------------------------|---|---|
| Ground State | Excited States                    |   |   |
| <b>4-Pr</b>  | ${}^3\text{H}_4 \rightarrow$      | ${}^3\text{P}_2, {}^3\text{P}_1, {}^3\text{P}_0, {}^1\text{D}_2$  | 451, 477, 491, 593 nm                           |
| <b>3-Pr</b>  | ${}^3\text{H}_4 \rightarrow$      | ${}^3\text{P}_2, {}^3\text{P}_1, {}^3\text{P}_0, {}^1\text{D}_2$  | 451, 477, 492, 593 nm                           |
| <b>4-Nd</b>  | ${}^4\text{I}_{9/2} \rightarrow$  | ${}^4\text{D}_{3/2}, {}^2\text{P}_{1/2}, {}^2\text{K}_{15/2}, {}^2\text{K}_{13/2}, {}^4\text{G}_{5/2}, {}^4\text{F}_{9/2}, {}^4\text{F}_{7/2}, {}^4\text{F}_{5/2}, {}^4\text{F}_{3/2}$  | 353, 432, 478, 529, 586, 681, 746, 803, 878 nm  |
| <b>3-Nd</b>  | ${}^4\text{I}_{9/2} \rightarrow$  | ${}^2\text{I}_{11/2}, {}^2\text{P}_{1/2}, {}^2\text{K}_{15/2}, {}^2\text{K}_{13/2}, {}^4\text{G}_{5/2}, {}^4\text{F}_{9/2}, {}^4\text{F}_{7/2}, {}^4\text{F}_{5/2}, {}^4\text{F}_{3/2}$ | 353, 433, 479, 529, 588, 682, 740, 804, 878 nm  |
| <b>4-Ho</b>  | ${}^5\text{I}_8 \rightarrow$      | $({}^5\text{G}, {}^3\text{H})_5, ({}^5\text{G}, {}^3\text{G})_5, {}^5\text{G}_6, {}^5\text{F}_2, {}^5\text{F}_3, {}^5\text{F}_4, {}^5\text{F}_5, {}^5\text{I}_5, {}^5\text{I}_6$        | 362, 419, 452, 474, 486, 539, 646, 892, 1150 nm |
| <b>3-Ho</b>  | ${}^5\text{I}_8 \rightarrow$      | $({}^5\text{G}, {}^3\text{H})_5, ({}^5\text{G}, {}^3\text{G})_5, {}^5\text{G}_6, {}^5\text{F}_2, {}^5\text{F}_3, {}^5\text{F}_4, {}^5\text{F}_5, {}^5\text{I}_5, {}^5\text{I}_6$        | 362, 420, 455, 475, 486, 539, 646, 891, 1149 nm |
| <b>4-Er</b>  | ${}^4\text{I}_{15/2} \rightarrow$ | ${}^4\text{G}_{11/2}, ({}^2\text{G}, {}^4\text{F})_{9/2}, {}^4\text{F}_{5/2}, {}^4\text{F}_{7/2}, {}^2\text{H}_{11/2}, {}^4\text{S}_{8/2}, {}^4\text{F}_{9/2}, {}^4\text{I}_{11/2}$     | 379, 408, 451, 488, 521, 543, 652, 971 nm       |
| <b>3-Er</b>  | ${}^4\text{I}_{15/2} \rightarrow$ | ${}^4\text{G}_{11/2}, ({}^2\text{G}, {}^4\text{F})_{9/2}, {}^4\text{F}_{5/2}, {}^4\text{F}_{7/2}, {}^2\text{H}_{11/2}, {}^4\text{S}_{8/2}, {}^4\text{F}_{9/2}, {}^4\text{I}_{11/2}$     | 379, 408, 450, 487, 520, 543, 649, 968 nm       |
| <b>4-Tm</b>  | ${}^3\text{H}_6 \rightarrow$      | ${}^1\text{D}_2, {}^1\text{G}_4, {}^3\text{F}_3, {}^3\text{H}_4, {}^3\text{H}_5$  | 360, 470, 691, 796, 1209 nm                     |

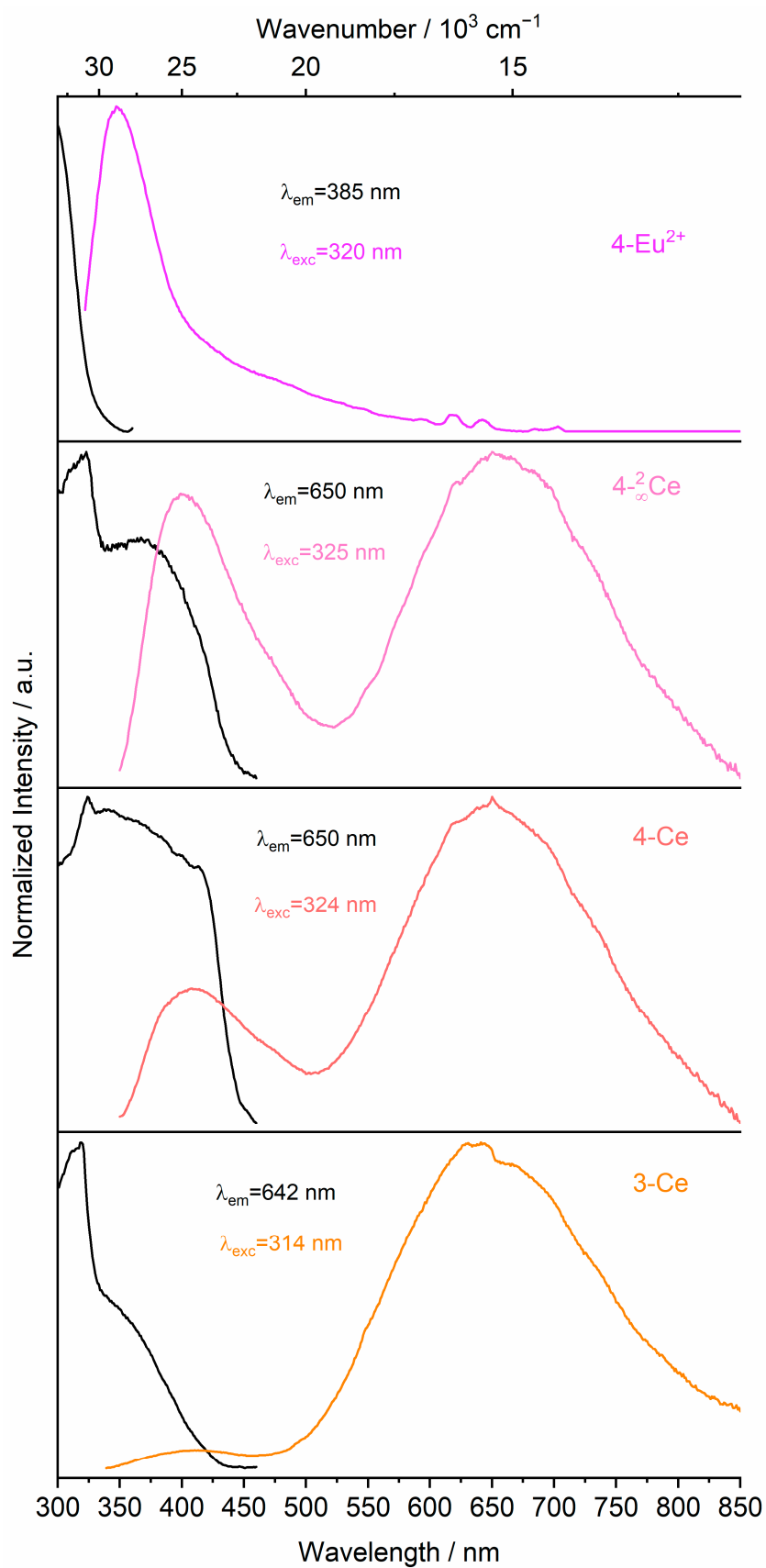


**Figure 7.** Normalized solid-state excitation (black) and emission (colored) spectra of  ${}^2_2[\text{Eu}(4\text{-PyPz})_2(\text{Py})_2]$  (**4-Eu<sup>2+</sup>**),  ${}^2_\infty[\text{Ce}(4\text{-PyPz})_3(\text{Py})]$  (**4-<sup>2</sup>Ce**),  ${}^3_\infty[\text{Ce}(4\text{-PyPz})_3]$  (**4-Ce**), and  ${}^3_\infty[\text{Ce}(3\text{-PyPz})_3]$  (**3-Ce**) at RT. Wavelengths for which the spectra were recorded are reported in the legends.

Although the excitation and emission spectra can provide a wealth of information, particularly about the coordination environment of the  $\text{Ln}^{3+}$  ions, it is uncommon to find the luminescence spectra for the  $\text{Tm}^{3+}$  and  $\text{Ho}^{3+}$ -based compounds. Nine-coordinated  $\text{Tm}^{3+}$  was only reported in three examples, and none of them investigated the photophysical properties, they mainly focused on the structural aspects [36,46,47]. In other cases, poor ligand-to-metal sensitization or back energy transfer occurs to allow only ligand-based luminescence, as in  $[\text{Tm}_2(\text{C}_{15}\text{H}_{11}\text{N}_3)_2(\text{C}_7\text{H}_4\text{BrO}_2)_4(\text{C}_2\text{O}_4)]$ , ( $\text{C}_{15}\text{H}_{11}\text{N}_3 = 2,2':6'2''$ -terpyridine and  $\text{C}_7\text{H}_4\text{BrO}_2 = p$ -bromobenzoic acid) [15],  $\text{Tm}(\text{bfa})_3\text{phen}$ , ( $\text{bfa} = 4,4,4$ -trifluoro-1-phenyl-1,3-butanedione,  $\text{phen} = 1,10$ -phenanthroline) [12], and  $\text{Tm}(\text{ppa})_3 \cdot 2\text{H}_2\text{O}$ , ( $\text{ppa} = 3$ -phenyl-2,4-pentanedionate) [13], where a significant ligand emission dominates the spectrum in addition to a single spectral band for the  $\text{Tm}^{3+}$ . Even nonefficient ligand sensitization with only a ligand emission band in the emission spectra was shown for  $[(\text{Tm}(\text{TC})_3(\text{H}_2\text{O})_2) \cdot (\text{HPy} \cdot \text{TC})]_n$ , ( $\text{TC} = 2$ -thiophenecarboxylate and  $\text{HPy} = \text{pyridinium cation}$ ) [16]. In contrast, very good ligand-to-metal sensitization is observed for  ${}^3_{\infty}[\text{Tm}(4\text{-PyPz})_3]$  (**4-Tm**) (Figure 8). The transitions  ${}^1\text{G}_4 \rightarrow {}^3\text{H}_6$ ,  ${}^3\text{F}_4$ ,  ${}^3\text{H}_5$ , and  ${}^3\text{H}_4$  are readily observable at 480, 650, 787, and 1192 nm, respectively.

For  ${}^3_{\infty}[\text{Ho}(4\text{-PyPz})_3]$  (**4-Ho**) and  ${}^3_{\infty}[\text{Ho}(3\text{-PyPz})_3]$  (**3-Ho**), the  ${}^5\text{F}_5 \rightarrow {}^5\text{I}_8$  is observed at 648 nm in addition to the NIR transition  ${}^5\text{I}_6 \rightarrow {}^5\text{I}_8$  at 1155 nm. An additional NIR transition appears for **4-Ho** at 983, corresponding to the transition  ${}^5\text{F}_5 \rightarrow {}^5\text{I}_7$  and indicating more efficient ligand sensitization than in reported cases, such as  $[(\text{Ho}(\text{TC})_3(\text{H}_2\text{O})_2) \cdot (\text{HPy} \cdot \text{TC})]_n$  with only ligand emission observable in the emission spectra [16]. The  $\text{Ho}^{3+}$ -based emission observed for both **3-Ho** and **4-Ho** is stronger than that of  ${}^2_{\infty}[\text{Ho}_2(3\text{-PyPzH})_3\text{Cl}_6] \cdot 2\text{MeCN}$  [14], which may be due to the absence of the vibrational energy of the chloride ligands.

For  ${}^3_{\infty}[\text{Pr}(4\text{-PyPz})_3]$  (**4-Pr**) and  ${}^3_{\infty}[\text{Pr}(3\text{-PyPz})_3]$  (**3-Pr**) (Figure 8), the highest intensity for the  $\text{Pr}^{3+}$ -based emission is found at 655 nm, corresponding to  ${}^3\text{P}_0 \rightarrow {}^3\text{F}_2$ . NIR emission bands can also be observed at 738 and 1048 nm for **4-Pr** and at 736 and 1038 nm for **3-Pr**, corresponding to the transitions  ${}^3\text{P}_0 \rightarrow {}^3\text{F}_4$  and  ${}^1\text{D}_2 \rightarrow {}^3\text{F}_4$ . Despite the ligand-based emission in **4-Pr** and **3-Pr** being more dominated than for the reported  ${}^1_{\infty}[\text{Pr}(2\text{-PyPz})_3]$  [32], the  $\text{Pr}^{3+}$ -based transitions are more characteristic than for other published cases, such as  ${}^1_{\infty}[\text{PrCl}_3(\text{ptpy})]$  and  $[\text{PrCl}_3(\text{ptpy})(\text{py})]$ ,  $\text{ptpy} = 4'$ -phenyl-2,2':6',2''-terpyridine) [48].

For  ${}^3_{\infty}[\text{Er}(4\text{-PyPz})_3]$  (**4-Er**) and  ${}^3_{\infty}[\text{Er}(3\text{-PyPz})_3]$  (**3-Er**), the NIR transition  ${}^4\text{I}_{13/2} \rightarrow {}^4\text{I}_{15/2}$  is observed at about 1510 nm and the VIS transition at about 545 nm can also be observed for **4-Er** at RT and 77 K, while at 77 K for **3-Er**. Both **4-Er** and **3-Er** show Stark-level splitting in the emissive transitions in contrast, e.g., to the reported  ${}^1_{\infty}[\text{LnCl}_3(\text{bipy})(\text{py})_2]\text{py}$ , which shows no fine splitting [48].

For the NIR emitters  ${}^3_{\infty}[\text{Nd}(4\text{-PyPz})_3]$  (**4-Nd**) and  ${}^3_{\infty}[\text{Nd}(3\text{-PyPz})_3]$  (**3-Nd**), the transitions  ${}^4\text{F}_{3/2} \rightarrow {}^4\text{I}_{j/2}$ , ( $j = 9, 11, 13$ ) are observed at about 915, 1065, and 1345 nm [11].

Generally, for the VIS–NIR and the NIR emitters, the emissive energy levels of the  $\text{Ln}^{3+}$ -based transitions are populated by an antenna effect between the pyridylpyrazolate-based ligands and the lanthanide ions, which leads to ligand-to-metal energy transfer, as observed for 2-PyPzH [32] and 4,4'-bipyridine (bipy) [49].

The ligands' fluorescence emission band has lifetimes of 6.07 ns for 4-PyPzH and 3.4 ns for 3-PyPzH [33] which are shortened by coordination with different  $\text{Ln}^{3+}$  ( $\tau = 0.93$ –1.04; Table S14). The lifetime increases with decreasing the temperature to 77 K, especially for 4-Nd, which increases from 0.93(2) ns at RT to 3.04(9) ns at 77 K due to the decrease in thermal quenching. See the Supplementary Materials for half-page size absorption and photoluminescence spectra with designated 4f–4f transitions for the investigated compounds (Figures S10–S37).

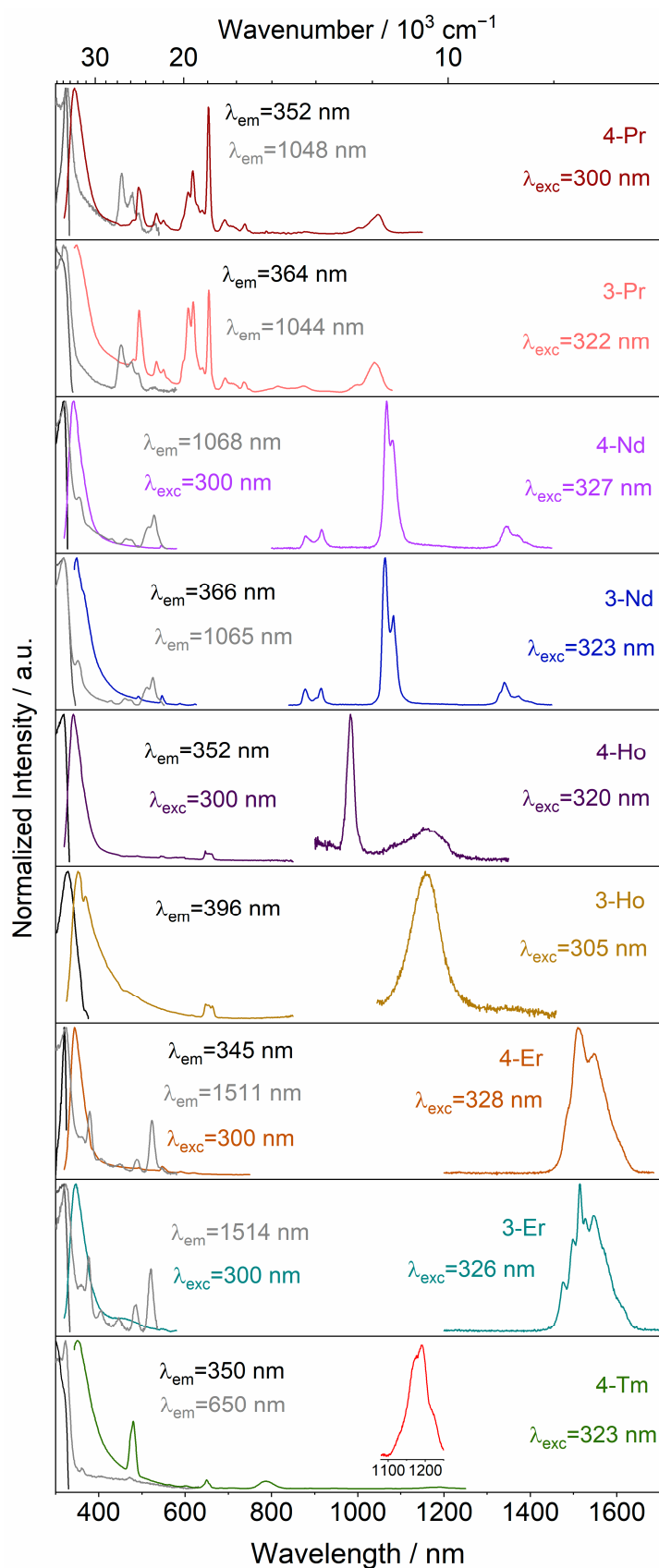
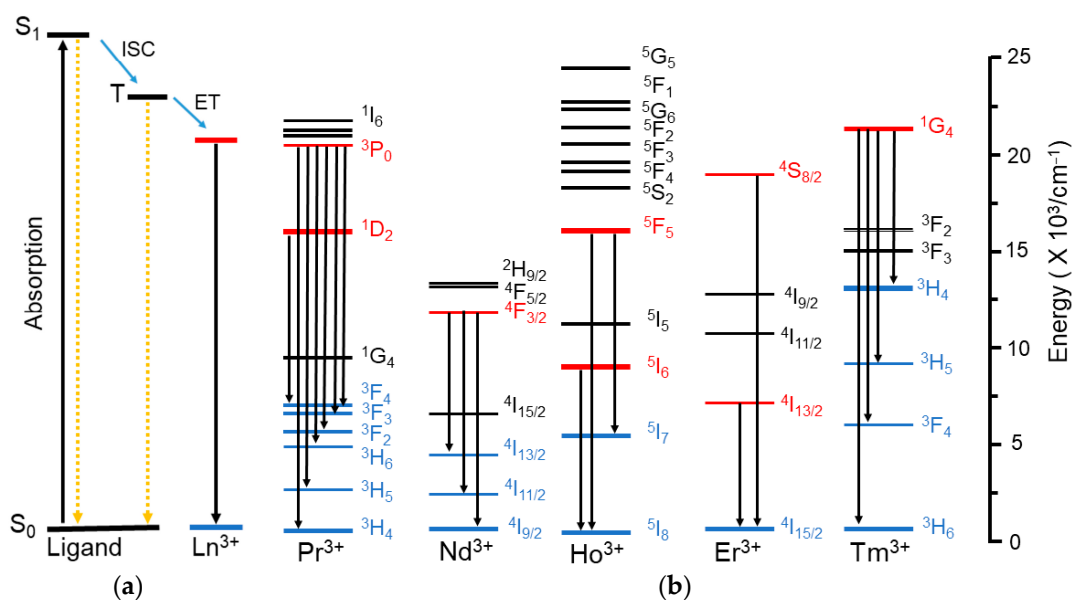


**Figure 8.** Normalized solid-state excitation (black) and emission spectra (colored) of  ${}^3_{\infty}[\text{Ln}(4\text{-PyPz})_3]$ , (4, Ln = Pr, Nd, Ho, Er, Tm) and  ${}^3_{\infty}[\text{Ln}(3\text{-PyPz})_3]$ , (3, Ln = Pr, Nd, Ho, Er) at RT. Wavelengths, for which the spectra were recorded, are reported in the legends.

### 2.2.3. Mechanism of Energy Transfer

To explain and understand the observed spectral results, a schematic diagram (Scheme 2) is shown, depicting the primary energy levels involved and the main energy transfer and relaxation pathways during the sensitization of lanthanide luminescence via the ligands. The ligands absorb energy and become excited from the singlet  $S_0$  ground state to the singlet  $S_1$  excited state by the absorption of visible light. The energy of the  $S_1$  excited state is then transferred to the triplet-excited state (T) of the ligands through intersystem crossing (ISC). Competing processes include ligand fluorescence and nonradiative deactivation of the excited singlet state. Subsequently, the excitation energy is transferred to the excited 4f levels of the  $\text{Ln}^{3+}$  ions, resulting in the respective lanthanide ion emission to the respective 4f ground state [50]. According to Dexter's theory [51], the energy gap between the first excited energy level of the  $\text{Ln}^{3+}$  ions and the energy level of the triplet state of the respective ligand is important for an efficient energy transfer. If the energy gap is too large, the overlap between the ligand and the  $\text{Ln}^{3+}$  is reduced, and as a result, the energy transfer decreases sharply. On the other hand, if the energy gap is too small, energy transfer also occurs from the  $\text{Ln}^{3+}$  back to the resonance levels of the triplet states of the ligands, which also reduces the 4f-based emission.



**Scheme 2.** (a) The Energy transfer mechanism; (b) energy level diagrams of  $\text{Pr}^{3+}$ ,  $\text{Nd}^{3+}$ ,  $\text{Ho}^{3+}$ ,  $\text{Er}^{3+}$ , and  $\text{Tm}^{3+}$  ions.

In this study, the triplet-state energy levels of 4-PyPz<sup>-</sup> and 3-PyPz<sup>-</sup> were investigated by deduction from the phosphorescence spectra of the Gd-based coordination polymers and calculated to be 23,640 and 23,250  $\text{cm}^{-1}$ , respectively [33]. This analogy is confirmed for 4-PyPz<sup>-</sup> through the spectra of 4-La, as discussed before. The discussed 4f emission bands of the respective Ln-based CPs indicate that the triplet states of the ligands are suitable for a transfer of the absorbed light to the lanthanide ions via such an antenna effect. For instance, the energy difference ( $\Delta E$ ) between the ligand triplet state of 4-PyPz<sup>-</sup> ( $\sim 23,640 \text{ cm}^{-1}$ ) and the energetic positions of  $\text{Tm}^{3+}$  ( $1G_4 = \sim 21,300 \text{ cm}^{-1}$ ) results in an  $\Delta E$  value in the optimal range.  $\text{Pr}^{3+}$  is slightly more complicated because it has two emission levels ( $3P_0$  and  $1D_2$ ). By considering the  $3P_0$  level as the main acceptor level with an energetic position of  $\sim 20,475 \text{ cm}^{-1}$  [11], the  $\Delta E$  values are calculated as 3165 and 2775 for 4-Pr and 3-Pr, respectively, both also being in the optimal range. For  $\text{Ho}^{3+}$ , the  $5F_4$ ,  $5S_2$ , and  $5F_5$  levels are the main acceptor levels, and the emission from the  $5F_5$  and  $5I_6$  levels can partially be the result of a relaxation of the upper levels followed by transitions to the lower levels to give the characteristic NIR emission of the  $\text{Ho}^{3+}$  ion [52].

### 2.3. Magnetic Properties

Direct current (DC) magnetic susceptibility measurements were performed for  ${}^3_{\infty}[\text{Ln}(\text{3-PyPz})_3]$ , Ln = Ho (**3-Ho**), Er (**3-Er**) in a temperature range of 3 to 300 K and a magnetic field of 1T. As a link to the reported isotopic series of  ${}^3_{\infty}[\text{Ln}(\text{3-PyPz})_3]$ , Ln = Sm, Eu, Gd, Tb, Dy [33], the DC magnetic susceptibility measurements of  ${}^3_{\infty}[\text{Dy}(\text{3-PyPz})_3]$  (**3-Dy**) were also performed.

The temperature dependence of the product of  $\chi T$  for all samples can be observed in Figure 9. At room temperature, the  $\chi_M T$  ( $\chi_M$  = molar magnetic susceptibility) values are 15.03, 14.05, and 10.70 for **3-Dy**, **3-Ho**, and **3-Er**, respectively. These experimental data are in satisfactory agreement with the theoretical values for the corresponding noninteracting  $\text{Dy}^{3+}$  ( ${}^6\text{H}_{15/2}$ ,  $S = 5/2$ ,  $L = 5$ ,  $g = 4/3$ ,  $\chi T = 14.17 \text{ cm}^3 \text{ K mol}^{-1}$ ),  $\text{Ho}^{3+}$  ( ${}^5\text{I}_8$ ,  $S = 5/2$ ,  $L = 6$ ,  $g = 5/4$ ,  $\chi T = 14.07 \text{ cm}^3 \text{ K mol}^{-1}$ ), and  $\text{Er}^{3+}$  ( ${}^4\text{I}_{15/2}$ ,  $S = 3/2$ ,  $L = 6$ ,  $g = 6/5$ ,  $\chi T = 11.48 \text{ cm}^3 \text{ K mol}^{-1}$ ) [53].

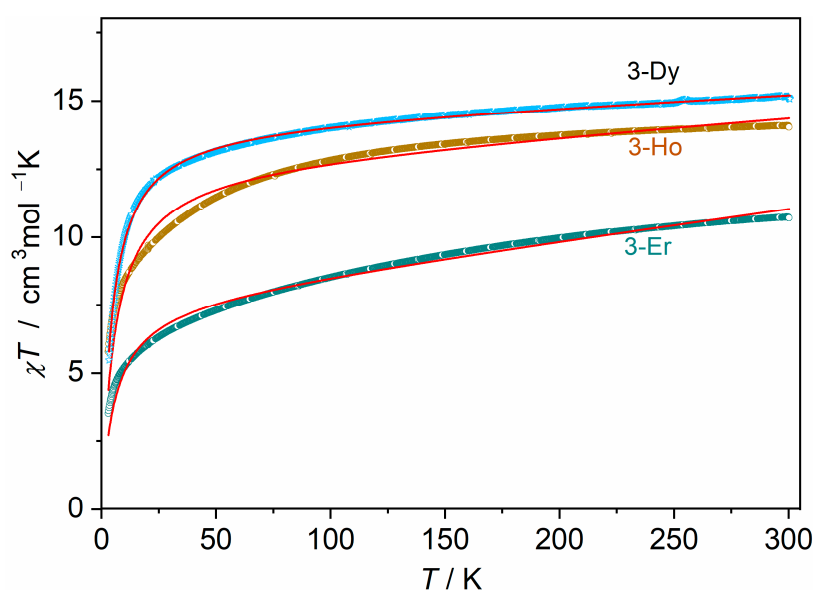


**Figure 9.** Variable temperature magnetic susceptibilities of  ${}^3_{\infty}[\text{Ln}(\text{4-PyPz})_3]$ , (Ln = Dy, Er), and  ${}^3_{\infty}[\text{Ho}(\text{3-PyPz})_3]$  (**3-Ho**) in a temperature range from 3 to 300 K and a magnetic field of 1T.

For **3-Dy**, **3-Ho**, and **3-Er**, a monotonic slow decrease in the  $\chi_M T$  product was observed upon cooling, which could be related to thermal depopulation within the  $m_J$  levels of the ground  ${}^6\text{H}_{15/2}$ ,  ${}^5\text{I}_8$ , and  ${}^4\text{I}_{15/2}$  multiplet, respectively. In addition, the  $\chi_M T$  vs  $T$  plot did not display abrupt changes, which suggests a lack of magnetic interactions down to 45, 75, and 80 K, with  $\chi_M T$  reaching  $3.01$ ,  $5.79$ , and  $3.49 \text{ cm}^3 \text{ K mol}^{-1}$ , respectively, because of the efficient magnetic isolation of lanthanide centers in the crystal lattice.

The data were fitted for **3-Dy**, **3-Ho**, and **3-Er** in the given temperature range with an effective magnetic moment  $\mu_{\text{eff}}$  of 10.651(2), 10.09(1), and 7.855(9)  $\mu\text{B}$  and a Weiss constant  $\theta$  of  $-4.41(1)$ ,  $-5.77(7)$ , and  $-5.72(8)$  K, as well as a temperature-independent paramagnetic susceptibility  $\chi_0$  of  $4.03(3) \times 10^{-3}$ ,  $6.18(2) \times 10^{-3}$ , and  $11.52(8) \times 10^{-3} \text{ cm}^3 \text{ mol}^{-1}$ . The small, negative Weiss constants  $\theta$  are the results of spin-orbit coupling as well as the crystal field effect [54,55].

## 3. Materials and Methods

### 3.1. General Procedures

3-(4-pyridyl)pyrazole (4-PyPzH) and 3-(3-pyridyl)pyrazole (3-PyPzH) were synthesized as reported in the literature [56,57]. Lanthanide metals (holmium: 99.9%, Chempur, Karlsruhe, Germany; rest: >99.99%, Smart Elements, Vienna, Austria) were purchased and used as received. Pyridine (Py), dichloromethane (DCM), and cyclohexane (Cy) were

purified by distillation and dried by standard procedures. All syntheses involving lanthanide elements were performed under argon or using vacuum lines, gloveboxes (MBraun Labmaster SP, Innovative Technology PureLab, Garching, Germany), Schlenk tubes, and Duran<sup>®</sup> glass ampoules (outer Ø 10 mm, wall thickness 1.5 mm). The solid reactants for the solvothermal reactions were mixed and sealed together with the solvent in an ampoule under reduced pressure ( $p = 1.0 \times 10^{-3}$  mbar) after freezing the solvent with liquid nitrogen. Subsequently, the prepared ampoules were placed in heating furnaces based on Al<sub>2</sub>O<sub>3</sub> tubes with Kanthal wire resistance heating and NiCr/Ni (Eurotherm 2416) temperature control elements, for which temperature programs and working steps according to the specific synthesis methods were used. After the solvents had been removed, the solid raw products were dried at RT in a dynamic vacuum ( $p = 1.0 \times 10^{-3}$  mbar) before further steps. The bulk materials were characterized by PXRD and CHN analysis. The prepared 3D frameworks and 2D networks are air sensitive due to the known oxophilic behavior of the Ln-based CPs. It is expected that the CPs are insoluble in common organic solvents. We think the photostability tests are not significant in the possible applications of these synthesized CPs.

### 3.2. X-ray Crystallography

SCXRD determinations were performed on a Bruker AXS D8 Venture diffractometer (Karlsruhe, Germany) equipped with dual I $\mu$ S microfocus sources, a collimating Quazar multilayer mirror, a Photon 100 detector, and an Oxford Cryosystems 700 low-temperature system (Mo-K $\alpha$  radiation;  $\lambda = 71.073$  pm). The structures were solved with direct methods and refined with the least squares method implemented in ShelX [58,59]. All nonhydrogen atoms were refined anisotropically. Hydrogen atoms were assigned to idealized geometric positions and included in structure factor calculations. Further, a ligand anion (4-PyPz<sup>-</sup>) and the pyridine solvent in the asymmetric unit of **4-Yb** and **4-Lu** were found to be fully disordered and were refined with the help of restraints to achieve a proper structural model. For polymers **4-La**, **4-Ce**, **4-Pr**, **4-Nd**, **4-Ho**, and **4-Er**, the SQUEEZE [60] algorithm in PLATON [61–64] was used to include a bulk solvent model in the refinement. Two voids per unit cell were identified with SQUEEZE. The average volume was found to be  $135 \times 10^6$  pm<sup>3</sup> for each void. The equivalent of 8 electrons for (**4-La**, **4-Ce**, **4-Pr**), 10 for (**4-Ho**), and 12 for (**4-Nd**) electrons per unit cell was also identified. ToposPro program package was used to determine the topology of the polymers [65]. Depictions of the crystal structures were created with Diamond [66]. The crystal structures have been deposited to the Cambridge Crystallographic Data Center (CCDC) as supplementary publication No. 2237763 (**4-Eu**<sup>2+</sup>), 2237764 (**4- $\infty$ -Tm**), 2237765 (**4-Yb**), 2237766 (**4-Lu**), 2237767 (**4-La**), 2237768 (**4-Ce**), 2237769 (**4-Pr**), 2237770 (**4-Nd**), 2237771 (**4-Ho**), 2237772 (for **4-Er**), 2237773 (**3-Ce**), 2237774 (**3-Pr**), 2237775 (**3-Nd**), 2237776 (**3-Ho**), 2237777 (for **3-Er**), and 2237778 (**3-Tm**). Crystallographic data and selected interatomic distances are listed in Tables S1–S11 for the investigated compounds.

PXRD analyses of the investigated compounds were carried out on a Stoe Stadi P diffractometer (Darmstadt, Germany) with a focusing Ge(111) monochromator and a Dectris Mythen 1K strip detector in Debye–Scherrer geometry. All powder samples were ground in a mortar and filled into Lindemann glass capillaries with 0.3 mm diameter under an inert gas atmosphere. All samples were measured in transmission geometry with Cu-K $\alpha$  radiation ( $\lambda = 154.056$  pm). Data collection was performed using the Stoe Powder Diffraction Software Package WinXPOW V3.0.2.1 and Pawley fits on the data were performed using TOPAS Academic V7 [67]. The data are presented in Figures 5 and S3–S9 in addition to Table S12.

### 3.3. Spectroscopical Investigations

#### 3.3.1. Absorption Spectra

The UV–Vis–NIR absorption spectra were measured on solid-state products using a standard Agilent Cary 5000 UV–VIS–NIR spectrophotometer (Agilent Technologies,

Waldbronn, Germany) with a Praying Mantis accessory (Harrick Scientific Instruments, New York, NY, USA), which had been mounted and aligned for use with the DRP-ASC ambient chamber. The source, detector, and grating changeovers were at the standard position of 350, 800, and 800 nm, respectively, for all studied compounds except  $4-^2_{\infty}\text{Ce}$ ,  $4\text{-Nd}$ ,  $4\text{-Tm}$ , and  $3\text{-Nd}$ , the detector and grating changeovers were set to 850 nm, while 750 nm for  $3\text{-Er}$ . For  $4\text{-Eu}^{2+}$ ,  $4-^2_{\infty}\text{Ce}$ ,  $4\text{-Ce}$ ,  $4\text{-Nd}$ ,  $4\text{-Tm}$ ,  $3\text{-Ce}$ , and  $3\text{-Nd}$ , the source was set to 320, 450, 330, 340, 335, 320, and 340 nm, respectively. The reference spectrum was collected on PTFE and the reference and samples were packed in the ambient chamber within the glovebox under inert conditions.

### 3.3.2. Photoluminescence Spectroscopy

The excitation and emission spectra were recorded for ground solid samples after filling them in quartz glass tubes under argon. The measurements were performed at room temperature as well as 77 K (latter using the liquid nitrogen-filled assembly FL-1013 of HORIBA) with a HORIBA Jobin Yvon Spex Fluorolog 3 spectrometer (Horiba-Jobin Yvon, Oberursel, Germany) equipped with a 450 W Xe short-arc lamp (USHIO INC., Tokyo, Japan), double-grated excitation, and emission monochromators, and a photomultiplier tube (R928P) using the FluoroEssence™ software V3.9. Excitation and emission spectra were corrected for the spectral response of the monochromators and the detector using spectral corrections provided by the constructor. In addition, a photodiode reference detector was used to correct the excitation spectra for the spectral distribution of the lamp intensity. An R5509-73 detector was used to collect the data in the NIR region. When required, the collection of the data was performed using an edge filter (Newport 20CGA-345, 395, 495 for the visible region and Reichmann Optics RG 830 long pass for the NIR region). Emission spectra with gating were recorded using a xenon flashlamp with a pulse repetition rate of 41 ms.

Photoluminescence overall decay process times were determined using the above-mentioned HORIBA Jobin Yvon Spex Fluorolog 3 spectrometer equipped with a dual lamp housing (FL-1040A), a UV xenon flashlamp (Exelitas FX-1102), and a TCSPC (time-correlated single-photon counting) upgrade, or picosecond pulsed laser diode. Emission decays were recorded using DataStation software V2.7. Exponential tail fitting was used for the calculation of resulting intensity decay using Decay Analysis Software 6. The quality of the fit was confirmed by  $\chi^2$  values being below 1.2.

### 3.4. PPMS Magnetic Measurements

Magnetic data were obtained with the application of the VSM option of a Quantum Design physical property measurement system (ppms). The data were corrected with respect to the contribution of the polypropylen sample holder as well as the diamagnetic contribution of the sample through utilization of both experimental data and Pascal constants (increment method). The total magnetic susceptibility is comprised of different parts: the diamagnetic contribution  $\chi_{Diam.}$ , the Curie paramagnetic contribution  $\chi_{CW}$ , and a temperature-independent paramagnetic contribution  $\chi_0$ .

$$\chi_{tot.} = \chi_{Diam.} + \chi_{Param.} = \chi_{Diam.} + \chi_{CW} + \chi_0$$

The Curie paramagnetic part is the ratio of the Curie constant  $C$  and the modified temperature  $(T - \theta)$ .  $\theta$  is the Weiss temperature

$$\chi_{CW} = \frac{C}{T - \theta}$$

The Curie constant is given by the formula:

$$C = \mu_0 \frac{N_A \mu_B^2 n_{eff}^2}{3k_B}$$

with  $\mu_0$  = magnetic constant,  $N_A$  = Avogadro number,  $\mu_B$  = Bohr magneton,  $n_{eff}$  = effective magnetic moment,  $k_B$  = Boltzmann constant.

The molar Curie paramagnetic contribution of the susceptibility is:

$$\chi_{mol_{CW}} = \frac{N_A \mu_B^2 n_{eff}^2}{3k_B(T - \theta)}$$

Or:

$$\chi_{mol_{CW}} = 0.1250 \frac{n_{eff}^2}{T - \Theta} / \text{cm}^3 \text{mol}^{-1}$$

To calculate the molar paramagnetic contribution of the susceptibility, we used the equation:

$$\chi_{mol} = 0.1250 \frac{n_{eff}^2}{T - \Theta} + \chi_0 / \text{cm}^3 \text{mol}^{-1}$$

For the analysis of the data the OriginPro software V2021b (Academic) was used.

### 3.5. Synthesis

#### 3.5.1. Synthesis of ${}^2_{\infty}[\text{Eu}(\text{4-PyPz})_2(\text{Py})_2]$ ( $4\text{-Eu}^{2+}$ )

Freshly filed Eu metal (108.6  $\mu\text{mol}$ ) and an excess of 4-PyPzH ( $\text{C}_8\text{H}_7\text{N}_3$ , 220  $\mu\text{mol}$ ) were mixed with Py (0.6 mL) and sealed in an evacuated ampoule. The ampoule was heated to 185  $^\circ\text{C}$  in 1 h and maintained at this temperature for 72 h. The reaction mixture was then cooled to room temperature within 4 h. The excess ligand was washed away using a mixture of DCM and Cy. Suitable single crystals were selected for a SCXRD measurement.  $\text{C}_{26}\text{H}_{22}\text{N}_8\text{Eu}$  (598.47  $\text{g}\cdot\text{mol}^{-1}$ ): C 51.59 (calcd. 52.18); H 3.04 (3.71); N 19.49 (18.72)%. Yield: 83%. FT-IR (ATR, Figure S39):  $\bar{\nu} = 3036$  (w), 1065 (s), 1552 (w), 1522 (w), 1456 (w), 1439 (m), 1418 (w), 1404 (w), 1346 (w), 1293 (w), 1213 (m), 1187 (w), 1065 (w), 1044 (m), 999 (s), 963 (w), 951 (w), 925 (w), 871 (w), 830 (s), 761 (s), 690 (s), 659 (w), 614 (m), 532 (m), 451 (m)  $\text{cm}^{-1}$ .

#### 3.5.2. Synthesis of ${}^2_{\infty}[\text{Ln}(\text{4-PyPz})_3(\text{Py})]$ ( $4\text{-}{}^2_{\infty}\text{Ce}$ , $4\text{-}{}^2_{\infty}\text{Tm}$ )

The respective freshly filed Ln metal (81.4  $\mu\text{mol}$ ) and an excess of 4-PyPzH ( $\text{C}_8\text{H}_7\text{N}_3$ , 327.6  $\mu\text{mol}$ ) were mixed with Py and sealed in an evacuated ampoule. The ampoule was heated to 180  $^\circ\text{C}$  in 24 h then the temperature was raised to 240  $^\circ\text{C}$  within 48 h and maintained at this temperature for 72 h. The reaction mixture was then cooled to room temperature within 48 h. The excess ligand was washed away using a mixture of DCM and Cy. Suitable single crystals were selected for a SCXRD measurement.  $\text{C}_{29}\text{H}_{23}\text{N}_{10}\text{Ce}$  (651.67  $\text{g}\cdot\text{mol}^{-1}$ ): C 52.63 (calcd. 53.45); H 2.67 (3.06); N 22.16 (21.49)%. Yield: 83%. FT-IR (ATR, Figure S40):  $\bar{\nu} = 3085$  (w), 1698 (w), 1606 (s), 1523 (w), 1459 (w), 1440 (m), 1418 (w), 1347 (w), 1330 (w), 1295 (w), 1212 (s), 1099 (w), 1066 (w), 1047 (m), 1003 (s), 992 (m), 968 (w), 929 (m), 857 (w), 830 (m), 773 (s), 741 (w), 692 (s), 652 (m), 622 (w), 572 (m), 457 (s)  $\text{cm}^{-1}$ .

#### 3.5.3. Synthesis of ${}^2_{\infty}[\text{Ln}_2(\text{4-PyPz})_6]\text{Py}$ ( $4\text{-Yb}$ , $4\text{-Lu}$ )

Freshly filed Yb (68.6  $\mu\text{mol}$ ) and an excess of 4-PyPzH ( $\text{C}_8\text{H}_7\text{N}_3$ , 275.6  $\mu\text{mol}$ ) were mixed with Py and sealed in an evacuated ampoule. The ampoule was heated to 180  $^\circ\text{C}$  in 24 h then the temperature was raised to 230  $^\circ\text{C}$  within 48 h and maintained at this temperature for 72 h. The reaction mixture was then cooled to room temperature within 48 h. Suitable single crystals were selected for a SCXRD measurement.

#### 3.5.4. Synthesis of ${}^3_{\infty}[\text{Ln}(\text{4-PyPz})_3]$ ( $4$ , Ln = La, Ce, Pr, Nd, Ho, Er, Tm)

A mixture of the respective freshly filed Ln metal (91.1  $\mu\text{mol}$ ) and excess 4-PyPzH ( $\text{C}_8\text{H}_7\text{N}_3$ , 275.6  $\mu\text{mol}$ ), in 0.3 mL pyridine, was sealed in an evacuated ampoule. The temperature was raised to 230  $^\circ\text{C}$  in 48 h, held for 96 h, and then lowered to room temperature

over a further 24 h. The excess ligand was washed away using a mixture of DCM and Cy. Colorless crystals were selected for SCXRD measurements.

${}^3\infty[\text{La}(\text{4-PyPz})_3]$  (**4-La**):  $\text{C}_{24}\text{H}_{18}\text{N}_9\text{La}$  (571.38  $\text{g}\cdot\text{mol}^{-1}$ ): C 49.53 (calcd. 50.45); H 2.89 (3.18); N 21.50 (22.06)%. Yield: 80%. FT-IR (ATR, Figure S41):  $\bar{\nu} = 3096$  (w), 1698 (w), 1607 (s), 1550 (w), 1526 (w), 1460 (w), 1447 (m), 1420 (w), 1348 (w), 1329 (w), 1215 (m), 1099 (w), 1066 (w), 1046 (m), 1005 (s), 968 (w), 927 (m), 831 (m), 763 (s), 739 (w), 694 (s), 652 (m), 527 (m), 459 (s)  $\text{cm}^{-1}$ .

${}^3\infty[\text{Ce}(\text{4-PyPz})_3]$  (**4-Ce**):  $\text{C}_{24}\text{H}_{18}\text{N}_9\text{Ce}$  (572.58  $\text{g}\cdot\text{mol}^{-1}$ ): C 49.81 (calcd. 50.34); H 3.26 (3.17); N 21.73 (22.02)%. Yield: 85%. FT-IR (ATR, Figure S42):  $\bar{\nu} = 3101$  (w), 1608 (s), 1526 (w), 1459 (w), 1447 (w), 1420 (w), 1348 (m), 1215 (m), 1066 (w), 1046 (m), 1006 (s), 969 (w), 927 (m), 831 (m), 763 (m), 739 (w), 695 (s), 652 (m), 527 (m), 460 (s)  $\text{cm}^{-1}$ .

${}^3\infty[\text{Pr}(\text{4-PyPz})_3]$  (**4-Pr**):  $\text{C}_{24}\text{H}_{18}\text{N}_9\text{Pr}$  (573.37  $\text{g}\cdot\text{mol}^{-1}$ ): C 49.39 (calcd. 50.27); H 3.07 (3.16); N 21.16 (21.99)%. Yield: 84%. FT-IR (ATR, Figure S43):  $\bar{\nu} = 3095$  (w), 1607 (s), 1526 (w), 1460 (w), 1446 (w), 1420 (w), 1348 (w), 1328 (w), 1215 (m), 1099 (w), 1067 (w), 1046 (m), 1006 (s), 969 (w), 927 (m), 831 (m), 762 (s), 739 (w), 694 (s), 652 (m), 527 (m), 460 (s)  $\text{cm}^{-1}$ .

${}^3\infty[\text{Nd}(\text{4-PyPz})_3]$  (**4-Nd**):  $\text{C}_{24}\text{H}_{18}\text{N}_9\text{Nd}$  (576.70  $\text{g}\cdot\text{mol}^{-1}$ ): C 49.33 (calcd. 49.98); H 2.73 (3.15); N 21.11 (21.86)%. Yield: 83%. FT-IR (ATR, Figure S44):  $\bar{\nu} = 3093$  (w), 1609 (s), 1526 (w), 1459 (w), 1447 (m), 1420 (w), 1348 (w), 1215 (m), 1074 (w), 1047 (m), 1007 (s), 969 (w), 928 (m), 831 (m), 771 (s), 763 (s), 740 (w), 696 (s), 652 (w), 527 (w), 461 (s)  $\text{cm}^{-1}$ .

${}^3\infty[\text{Ho}(\text{4-PyPz})_3]$  (**4-Ho**):  $\text{C}_{24}\text{H}_{18}\text{N}_9\text{Ho}$  (597.39  $\text{g}\cdot\text{mol}^{-1}$ ): C 47.44 (calcd. 48.25); H 2.75 (3.04); N 20.14 (21.10)%. Yield: 86%. FT-IR (ATR, Figure S45):  $\bar{\nu} = 3113$  (w), 1697 (w), 1609 (s), 1549 (w), 1526 (w), 1460 (w), 1446 (w), 1419 (w), 1348 (w), 1328 (w), 1297 (w), 1214 (m), 1101 (w), 1075 (w), 1048 (m), 1007 (s), 970 (w), 929 (m), 845 (w), 831 (m), 770 (s), 760 (s), 739 (m), 696 (s), 652 (m), 528 (m), 461 (s)  $\text{cm}^{-1}$ .

${}^3\infty[\text{Er}(\text{4-PyPz})_3]$  (**4-Er**):  $\text{C}_{24}\text{H}_{18}\text{N}_9\text{Er}$  (599.72  $\text{g}\cdot\text{mol}^{-1}$ ): C 48.85 (calcd. 48.07); H 3.34 (3.03); N 20.69 (21.02)%. Yield: 89%. FT-IR (ATR, Figure S46):  $\bar{\nu} = 3062$  (w), 1696 (w), 1609 (s), 1549 (w), 1526 (w), 1460 (w), 1446 (w), 1419 (w), 1348 (w), 1328 (w), 1214 (m), 1101 (w), 1076 (m), 1048 (m), 1008 (s), 971 (w), 929 (m), 831 (m), 770 (s), 759 (s), 739 (m), 697 (s), 652 (m), 528 (m), 461 (s)  $\text{cm}^{-1}$ .

${}^3\infty[\text{Tm}(\text{4-PyPz})_3]$  (**4-Tm**):  $\text{C}_{24}\text{H}_{18}\text{N}_9\text{Tm}$  (601.39  $\text{g}\cdot\text{mol}^{-1}$ ): C 48.90 (calcd. 47.93); H 3.11 (3.02); N 19.97 (20.96)%. Yield: 82%. FT-IR (ATR, Figure S47):  $\bar{\nu} = 3117$  (w), 1697 (w), 1609 (s), 1550 (w), 1527 (m), 1460 (m), 1447 (m), 1419 (w), 1349 (m), 1329 (w), 1296 (w), 1214 (s), 1102 (w), 1077 (m), 1049 (m), 1008 (s), 971 (w), 930 (m), 845 (w), 830 (s), 770 (s), 759 (s), 740 (m), 696 (s), 652 (m), 528 (m), 461 (s)  $\text{cm}^{-1}$ .

### 3.5.5. Synthesis of ${}^3\infty[\text{Ln}(\text{3-PyPz})_3]$ (3, Ln = Ce, Pr, Nd, Ho, Er)

A mixture of the respective freshly filed Ln metal (78.8  $\mu\text{mol}$ ) and an excess of 3-PyPzH ( $\text{C}_8\text{H}_7\text{N}_3$ , 240  $\mu\text{mol}$ ) together with 0.3 mL pyridine were sealed in an evacuated ampoule. The oven was heated to 180  $^\circ\text{C}$  in 24 h. Subsequently, the temperature was raised to 230  $^\circ\text{C}$  in 48 h. The temperature was held for 72 h and then lowered to room temperature over a further 48 h. Single crystals were selected for SCXRD measurements.

${}^3\infty[\text{Ce}(\text{3-PyPz})_3]$  (**3-Ce**):  $\text{C}_{24}\text{H}_{18}\text{N}_9\text{Ce}$  (572.58  $\text{g}\cdot\text{mol}^{-1}$ ): C 50.50 (calcd. 50.34); H 3.11 (3.17); N 21.16 (22.02)%. Yield: 83%. FT-IR (ATR, Figure S48):  $\bar{\nu} = 3085$  (w), 1596 (w), 1576 (m), 1509 (w), 1464 (m), 1453 (m), 1407 (m), 1359 (w), 1346 (w), 1250 (w), 1206 (m), 1186 (m), 1122 (w), 1099 (w), 1072 (m), 1039 (s), 963 (m), 928 (m), 859 (w), 818 (m), 779 (s), 716 (w), 702 (s), 656 (w), 635 (s), 510 (w), 461 (s)  $\text{cm}^{-1}$ .

${}^3\infty[\text{Pr}(\text{3-PyPz})_3]$  (**3-Pr**):  $\text{C}_{24}\text{H}_{18}\text{N}_9\text{Pr}$  (573.37  $\text{g}\cdot\text{mol}^{-1}$ ): C 49.35 (calcd. 50.27); H 2.63 (3.16); N 22.89 (21.99)%. Yield: 81%. FT-IR (ATR, Figure S49):  $\bar{\nu} = 2897$  (w), 1683 (m), 1596 (w), 1576 (w), 1508 (w), 1453 (m), 1407 (m), 1359 (w), 1345 (w), 1260 (w), 1249 (w), 1207 (m), 1186 (m), 1099 (w), 1074 (m), 1041 (s), 963 (m), 928 (m), 817 (w), 781 (s), 702 (s), 657 (w), 636 (s), 515 (w), 462 (s)  $\text{cm}^{-1}$ .

${}^3\infty[\text{Nd}(\text{3-PyPz})_3]$  (**3-Nd**):  $\text{C}_{24}\text{H}_{18}\text{N}_9\text{Nd}$  (576.70  $\text{g}\cdot\text{mol}^{-1}$ ): C 48.28 (calcd. 48.98); H 2.84 (3.15); N 21.39 (21.86)%. Yield: 80%. FT-IR (ATR, Figure S50):  $\bar{\nu} = 3085$  (w), 1576 (m), 1509 (w), 1465 (m), 1452 (m), 1408 (m), 1360 (m), 1347 (m), 1330 (w), 1249 (w), 1207 (m), 1186 (s),

1122 (w), 1099 (w), 1072 (m), 1041 (s), 963 (m), 928 (s), 818 (m), 779 (s), 717 (w), 702 (s), 656 (m), 636 (s), 509 (w), 463 (s)  $\text{cm}^{-1}$ .

${}^3_{\infty}[\text{Ho}(3\text{-PyPz})_3]$  (**3-Ho**):  $\text{C}_{24}\text{H}_{18}\text{N}_9\text{Ho}$  (597.39  $\text{g}\cdot\text{mol}^{-1}$ ): C 47.95 (calcd. 48.25); H 2.94 (3.04); N 20.16 (21.10)%. Yield: 86%. FT-IR (ATR, Figure S51):  $\bar{\nu}$  = 3086 (w), 1597 (w), 1577 (m), 1508 (w), 1465 (m), 1452 (m), 1408 (m), 1348 (m), 1248 (w), 1210 (m), 1187 (s), 1100 (w), 1075 (m), 1044 (s), 964 (m), 931 (m), 818 (m), 778 (s), 700 (s), 657 (m), 637 (s), 467 (s)  $\text{cm}^{-1}$ .

${}^3_{\infty}[\text{Er}(3\text{-PyPz})_3]$  (**3-Er**):  $\text{C}_{24}\text{H}_{18}\text{N}_9\text{Er}$  (599.72  $\text{g}\cdot\text{mol}^{-1}$ ): C 48.86 (calcd. 48.07); H 2.69 (3.03); N 20.77 (21.02)%. Yield: 87%. FT-IR (ATR, Figure S52):  $\bar{\nu}$  = 3086 (w), 1577 (w), 1508 (w), 1465 (w), 1453 (w), 1408 (w), 1348 (w), 1248 (w), 1210 (w), 1187 (m), 1100 (w), 1077 (m), 1045 (s), 964 (m), 931 (m), 818 (w), 780 (s), 700 (m), 657 (w), 637 (m), 513 (w), 468 (s)  $\text{cm}^{-1}$ .

### 3.5.6. Single Crystal of ${}^3_{\infty}[\text{Tm}(3\text{-PyPz})_3]$ (**3-Tm**):

Freshly filed Tm (68.7  $\mu\text{mol}$ ) and excess of 4-PyPzH ( $\text{C}_8\text{H}_7\text{N}_3$ , 210.5  $\mu\text{mol}$ ) were mixed with Py and sealed in an evacuated ampoule. The ampoule was heated to 180  $^\circ\text{C}$  in 1 h then the temperature was raised to 240  $^\circ\text{C}$  within 48 h and maintained at this temperature for 168 h. The reaction mixture was then cooled to room temperature within 48 h. Suitable single crystals were selected for a SCXRD measurement.

## 4. Conclusions

Divalent europium in the 2D network  ${}^2_{\infty}[\text{Eu}(4\text{-PyPz})_2(\text{Py})_2]$  and the trivalent lanthanide containing 3D frameworks  ${}^3_{\infty}[\text{Ln}(4\text{-PyPz})_3]$  and  ${}^3_{\infty}[\text{Ln}(3\text{-PyPz})_3]$ , Ln =  $\text{Ce}^{3+}$ ,  $\text{Pr}^{3+}$ ,  $\text{Nd}^{3+}$ ,  $\text{Ho}^{3+}$ ,  $\text{Er}^{3+}$ ,  $\text{Tm}^{3+}$ ,  ${}^3_{\infty}[\text{La}(4\text{-PyPz})_3]$ , as well as the 2D networks  ${}^2_{\infty}[\text{Ln}(4\text{-PyPz})_3(\text{Py})]$ , Ln =  $\text{Ce}^{3+}$ ,  $\text{Tm}^{3+}$  and  ${}^2_{\infty}[\text{Ln}_2(4\text{-PyPz})_6]\text{Py}$ , Ln =  $\text{Yb}^{3+}$ ,  $\text{Lu}^{3+}$  were synthesized by redox reactions between the elemental lanthanide and the ligand 3-(4-pyridyl)pyrazole (4-PyPzH) or 3-(3-pyridyl)pyrazole (3-PyPzH). The 18 coordination polymers were synthesized in a solvothermal processes in pyridine, in which the latter can act as a co-ligand. Uncommon NIR emission for  $\text{Tm}^{3+}$  and  $\text{Ho}^{3+}$  was detected along with additional  $\text{Pr}^{3+}$ ,  $\text{Er}^{3+}$ , and  $\text{Nd}^{3+}$  NIR emission benefited from a good ligand sensitizing effect. In addition,  $\text{Ce}^{3+}$ -based coordination polymers showed strong reductions in the 5d excited state, resulting in a distinctive pink to orange emission. Magnetic studies conducted with direct current (DC) showed magnetic isolation of the lanthanide centers in  ${}^3_{\infty}[\text{Ln}(3\text{-PyPz})_3]$ , Ln = Dy, Ho, Er. In summary, coordination polymers with pyridylpyrazolate ligands as N-donors can display a wide range of photoluminescent properties.

**Supplementary Materials:** The following supporting information can be downloaded at: <https://www.mdpi.com/article/10.3390/chemistry5020069/s1>, additional experimental details; Tables S1–S11: Crystallographic data and selected interatomic distances (pm) and angles ( $^\circ$ ) of  ${}^2_{\infty}[\text{Eu}(4\text{-PyPz})_2(\text{Py})_2]$  (**4-Eu<sup>2+</sup>**),  ${}^2_{\infty}[\text{Ln}_2(4\text{-PyPzH})_6]\text{Py}$ , Ln = Yb (**4-Yb**) and Lu (**4-Lu**),  ${}^2_{\infty}[\text{Tm}(4\text{-PyPz})_3(\text{Py})]$  (**4-<sup>2</sup>Tm**),  ${}^3_{\infty}[\text{Ln}(4\text{-PyPz})_3]$ , Ln = La (**4-La**), Ce (**4-Ce**), Pr (**4-Pr**), Nd (**4-Nd**), Ho (**4-Ho**), Er (**4-Er**), and  ${}^3_{\infty}[\text{Ln}(3\text{-PyPz})_3]$ , Ln = Ce (**3-Ce**), Pr (**3-Pr**), Nd (**3-Nd**), Ho (**3-Ho**), Er (**3-Er**), Tm (**3-Tm**); Figure S1: Extended coordination sphere of  $\text{Ce}^{3+}$  in  ${}^3_{\infty}[\text{Ce}(4\text{-PyPz})_3]$  (**4-Ce**) representing the series of isotopic framework compounds (**4**, Ln = La, Ce, Pr, Nd, Ho, Er, Tm). The coordination polyhedra around  $\text{Ce}^{3+}$  is indicated in green and the thermal ellipsoids describe a 50% probability level of the atoms. Symmetry operations: I  $x + 1/2, -y + 1/2, z + 1/2$  II  $-x + 3/2, y - 1/2, -z + 3/2$  III  $x + 1, y, z$ ; Figure S2: Extended coordination sphere of  $\text{Ce}^{3+}$  in  ${}^3_{\infty}[\text{Ce}(3\text{-PyPz})_3]$  (**3-Ce**) representing the series of isotopic framework compounds (**3**, Ln = Ce, Pr, Nd, Ho, Er, Tm). The coordination polyhedra around  $\text{Ce}^{3+}$  is indicated in green and the thermal ellipsoids describe a 50% probability level of the atoms. Symmetry operations: I  $-z + 1, x + 1/2, -y + 3/2$  II  $y - 1/2, -z + 3/2, -x + 1$  III  $x - 1/2, y, -z + 3/2$  IV  $y - 1/2, z, -x + 3/2$  V  $z - 1/2, x, -y + 3/2$ ; Figure S3: Comparison of the experimental X-ray powder diffraction pattern of  ${}^3_{\infty}[\text{Ln}(3\text{-PyPz})_3]$  (**3**, Ln = Pr, Nd, Ho, Er, Tm) at RT with the simulated pattern from the single-crystal X-ray data of  ${}^3_{\infty}[\text{Er}(3\text{-PyPz})_3]$  (**3-Er**) at 100 K; Figures S4–S8: Pawley refinement results for PXRD of  ${}^3_{\infty}[\text{Ln}(4\text{-PyPz})_3]$ , Ln = La (**4-La**), Pr (**4-Pr**), Nd (**4-Nd**), Ho (**4-Ho**), and Er (**4-Er**) showing the experimental data (black) together with the Pawley fit (red), the corresponding difference plot (blue), as well as hkl position markers (green); Table S12: Pawley refinement results for  ${}^2_{\infty}[\text{Eu}(4\text{-PyPz})_2(\text{Py})_2]$  (**4-Eu<sup>2+</sup>**),  ${}^2_{\infty}[\text{Ce}(4\text{-PyPz})_3(\text{Py})]$  (**4-<sup>2</sup>Ce**), and  ${}^3_{\infty}[\text{Ln}(4\text{-PyPz})_3]$  (**4**, Ln = La, Pr,

Nd, Ho, Er, Tm); Figure S9: Comparison of the experimental X-ray powder diffraction pattern of  ${}^2_{\infty}[\text{Tm}(\text{4-PyPz})_3(\text{Py})]$  (**4- ${}^2_{\infty}\text{Tm}$** ),  ${}^2_{\infty}[\text{Ln}_2(\text{4-PyPzH})_6\text{Py}]$ , Ln = Yb (**4- ${}^2_{\infty}\text{Yb}$** ) and Lu (**4- ${}^2_{\infty}\text{Lu}$** ) at RT with the respective simulated pattern from single-crystal X-ray data at 100 K; Figures S10–S23: Absorption spectra of 4-PyPzH,  ${}^2_{\infty}[\text{Eu}(\text{4-PyPz})_2(\text{Py})_2]$  (**4- ${}^2_{\infty}\text{Eu}^{2+}$** ),  ${}^2_{\infty}[\text{Ce}(\text{4-PyPz})_3(\text{Py})]$  (**4- ${}^2_{\infty}\text{Ce}$** ),  ${}^3_{\infty}[\text{Ln}(\text{4-PyPz})_3]$ , (**4**, Ln = Ce, Pr, Nd, Ho, Er, Tm) and  ${}^3_{\infty}[\text{Ln}(\text{3-PyPz})_3]$ , (**3**, Ln = Ce, Pr, Nd, Ho, Er) in the solid state at room temperature; Figure S24: Chromaticity coordinate diagram (CIE 1931) of the emission colors of  ${}^2_{\infty}[\text{Ce}(\text{4-PyPz})_3(\text{Py})]$  (**4- ${}^2_{\infty}\text{Ce}$** ),  ${}^3_{\infty}[\text{Ce}(\text{4-PyPz})_3]$  (**4- ${}^3_{\infty}\text{Ce}$** ) and  ${}^3_{\infty}[\text{Ce}(\text{3-PyPz})_3]$  (**3- ${}^3_{\infty}\text{Ce}$** ); Table S13: Chromaticity coordinates (x,y) for  ${}^2_{\infty}[\text{Ce}(\text{4-PyPz})_3(\text{Py})]$  (**4- ${}^2_{\infty}\text{Ce}$** ),  ${}^3_{\infty}[\text{Ce}(\text{4-PyPz})_3]$  (**4- ${}^3_{\infty}\text{Ce}$** ), and  ${}^3_{\infty}[\text{Ce}(\text{3-PyPz})_3]$  (**3- ${}^3_{\infty}\text{Ce}$** ); Figures S25–S38: Normalized excitation and emission spectra of  ${}^2_{\infty}[\text{Eu}(\text{4-PyPz})_2(\text{Py})_2]$  (**4- ${}^2_{\infty}\text{Eu}^{2+}$** ),  ${}^2_{\infty}[\text{Ce}(\text{4-PyPz})_3(\text{Py})]$  (**4- ${}^2_{\infty}\text{Ce}$** ),  ${}^3_{\infty}[\text{Ln}(\text{4-PyPz})_3]$ , (**4**, Ln = La, Ce, Pr, Nd, Ho, Er, Tm) and  ${}^3_{\infty}[\text{Ln}(\text{3-PyPz})_3]$ , (**3**, Ln = Ce, Pr, Nd, Ho, Er) at room temperature (top) and 77 K (bottom). Wavelengths at which the spectra were recorded are reported in the legends; Table S14: Photophysical data of  ${}^2_{\infty}[\text{Eu}(\text{4-PyPz})_2(\text{Py})_2]$  (**4- ${}^2_{\infty}\text{Eu}^{2+}$** ),  ${}^2_{\infty}[\text{Ce}(\text{4-PyPz})_3(\text{Py})]$  (**4- ${}^2_{\infty}\text{Ce}$** ),  ${}^3_{\infty}[\text{Ln}(\text{4-PyPz})_3]$ , (**4**, Ln = La, Ce, Pr, Nd, Ho, Er, Tm) and  ${}^3_{\infty}[\text{Ln}(\text{3-PyPz})_3]$ , (**3**, Ln = Ce, Pr, Nd, Ho, Er) in the solid state at room temperature and 77 K; Figures S39–S54: The infrared spectrum (ATR) of  ${}^2_{\infty}[\text{Eu}(\text{4-PyPz})_2(\text{Py})_2]$  (**4- ${}^2_{\infty}\text{Eu}^{2+}$** ),  ${}^2_{\infty}[\text{Ce}(\text{4-PyPz})_3(\text{Py})]$  (**4- ${}^2_{\infty}\text{Ce}$** ),  ${}^3_{\infty}[\text{Ln}(\text{4-PyPz})_3]$ , (**4**, Ln = La, Ce, Pr, Nd, Ho, Er, Tm),  ${}^3_{\infty}[\text{Ln}(\text{3-PyPz})_3]$ , (**3**, Ln = Ce, Pr, Nd, Ho, Er), 3-PyPzH, and 4-PyPzH.

**Author Contributions:** Conceptualization, K.M.-B. and H.Y.; methodology, H.Y.; software, H.Y. and J.B.; validation, H.Y.; formal analysis, H.Y. and C.P.; investigation, H.Y.; resources, I.V.T., F.K. and K.M.-B.; data curation, H.Y. and J.B.; writing—original draft preparation, H.Y.; writing—review and editing, H.Y., J.B., I.V.T., C.P., F.K. and K.M.-B.; visualization, H.Y.; supervision, K.M.-B.; project administration, K.M.-B. All authors have read and agreed to the published version of the manuscript.

**Funding:** This research was funded by the Deutsche Forschungsgemeinschaft DFG, grant No. MU-1562/7-2. H.Y. was awarded a PhD fellowship by the Egyptian Ministry of Higher Education (MoHE) and the German Academic Exchange Service (DAAD) within the German Egyptian Research Long-term Scholarship (GERLS) Program, 2017 (57311832), the funding agency is the German Academic Exchange Service Cairo. In the 14th round of applications, H.Y. was awarded a dissertation completion grant offered on the basis of JLU's Gender Equality Concept. The synthesis of the studied ligand was funded by the Russian Science Foundation (project No. 19–13–00272).

**Data Availability Statement:** CCDC 2237763 (**4- ${}^2_{\infty}\text{Eu}^{2+}$** ), 2237764 (**4- ${}^2_{\infty}\text{Tm}$** ), 2237765 (**4- ${}^2_{\infty}\text{Yb}$** ), 2237766 (**4- ${}^2_{\infty}\text{Lu}$** ), 2237767 (**4- ${}^2_{\infty}\text{La}$** ), 2237768 (**4- ${}^2_{\infty}\text{Ce}$** ), 2237769 (**4- ${}^2_{\infty}\text{Pr}$** ), 2237770 (**4- ${}^2_{\infty}\text{Nd}$** ), 2237771 (**4- ${}^2_{\infty}\text{Ho}$** ), 2237772 (for **4- ${}^2_{\infty}\text{Er}$** ), 2237773 (**3- ${}^3_{\infty}\text{Ce}$** ), 2237774 (**3- ${}^3_{\infty}\text{Pr}$** ), 2237775 (**3- ${}^3_{\infty}\text{Nd}$** ), 2237776 (**3- ${}^3_{\infty}\text{Ho}$** ), 2237777 (for **3- ${}^3_{\infty}\text{Er}$** ), and 2237778 (**3- ${}^3_{\infty}\text{Tm}$** ) contain the supplementary crystallographic data for this paper. These data can be obtained free of charge via <http://www.ccdc.cam.ac.uk/conts/retrieving.html> (or from the CCDC, 12 Union Road, Cambridge, CB2 1EZ, UK; Fax: +44 1223 336033; email: deposit@ccdc.cam.ac.uk).

**Conflicts of Interest:** The authors declare no conflict of interest.

## References

1. Millward, J.M.; Ariza de Schellenberger, A.; Berndt, D.; Hanke-Vela, L.; Schellenberger, E.; Waiczies, S.; Taupitz, M.; Kobayashi, Y.; Wagner, S.; Infante-Duarte, C. Application of europium-doped very small iron oxide nanoparticles to visualize neuroinflammation with MRI and fluorescence microscopy. *Neuroscience* **2017**, *403*, 136–144. [[CrossRef](#)]
2. Lenora, C.U.; Carniato, F.; Shen, Y.; Latif, Z.; Haacke, E.M.; Martin, P.D.; Botta, M.; Allen, M.J. Structural features of europium(II)-containing cryptates that influence relaxivity. *Chem. Eur. J.* **2017**, *23*, 15404–15414. [[CrossRef](#)]
3. Acharjya, A.; Corbin, B.A.; Prasad, E.; Allen, M.J.; Maity, S. Solvation-controlled emission of divalent europium salts. *J. Photochem. Photobiol. A* **2022**, *429*, 113892–113899. [[CrossRef](#)]
4. Dorenbos, P. Anomalous luminescence of  $\text{Eu}^{2+}$  and  $\text{Yb}^{2+}$  in inorganic compounds. *J. Phys. Condens. Matter* **2003**, *15*, 2645–2665. [[CrossRef](#)]
5. Qin, X.; Liu, X.; Huang, W.; Bettinelli, M.; Liu, X. Lanthanide-activated phosphors based on 4f-5d optical transitions: Theoretical and experimental aspects. *Chem. Rev.* **2017**, *117*, 4488–4527. [[CrossRef](#)] [[PubMed](#)]
6. Zurawski, A.; Mai, M.; Baumann, D.; Feldmann, C.; Müller-Buschbaum, K. Homoleptic imidazolate frameworks  ${}^3_{\infty}[\text{Sr}_{1-x}\text{Eu}_x(\text{Im})_2]$ —hybrid materials with efficient and tuneable luminescence. *Chem. Commun.* **2011**, *47*, 496–498. [[CrossRef](#)]
7. Kajdas, C.; Furey, M.J.; Ritter, A.L.; Molina, G.J. Triboemission as a basic part of the boundary friction regime. *Lubr. Sci.* **2002**, *14*, 223–254. [[CrossRef](#)]
8. Galimov, D.I.; Yakupova, S.M.; Vasilyuk, K.S.; Bulgakov, R.G. A novel gas assay for ultra-small amounts of molecular oxygen based on the chemiluminescence of divalent europium. *J. Photochem. Photobiol. A* **2021**, *418*, 113430–113437. [[CrossRef](#)]

9. Eliseeva, S.V.; Bünzli, J.-C.G. Lanthanide luminescence for functional materials and bio-sciences. *Chem. Soc. Rev.* **2010**, *39*, 189–227. [[CrossRef](#)]
10. Bünzli, J.C.G.; Piguet, C. Taking advantage of luminescent lanthanide ions. *Chem. Soc. Rev.* **2005**, *34*, 1048–1077. [[CrossRef](#)]
11. Carnall, W.T.; Fields, P.R.; Rajnak, K. Electronic energy levels in the trivalent lanthanide aquo ions. I.  $\text{Pr}^{3+}$ ,  $\text{Nd}^{3+}$ ,  $\text{Pm}^{3+}$ ,  $\text{Sm}^{3+}$ ,  $\text{Dy}^{3+}$ ,  $\text{Ho}^{3+}$ ,  $\text{Er}^{3+}$ , and  $\text{Tm}^{3+}$ . *J. Chem. Phys.* **1968**, *49*, 4424–4442. [[CrossRef](#)]
12. Feng, J.; Zhang, H.-J.; Song, S.-Y.; Li, Z.-F.; Sun, L.-N.; Xing, Y.; Guo, X.-M. Syntheses, crystal structures, visible and near-IR luminescent properties of ternary lanthanide ( $\text{Dy}^{3+}$ ,  $\text{Tm}^{3+}$ ) complexes containing 4,4,4-trifluoro-1-phenyl-1,3-butanedione and 1,10-phenanthroline. *J. Lumin.* **2008**, *128*, 1957–1964. [[CrossRef](#)]
13. Serra, O.A.; Nassar, E.J.; Calefi, P.S.; Rosa, I.L.V. Luminescence of a new  $\text{Tm}^{3+}$   $\beta$ -diketonate compound. *J. Alloys Compd.* **1998**, *275–277*, 838–840. [[CrossRef](#)]
14. Youssef, H.; Schäfer, T.; Becker, J.; Sedykh, A.E.; Basso, L.; Pietzonka, C.; Taydakov, I.V.; Kraus, F.; Müller-Buschbaum, K. 3D-Frameworks and 2D-networks of lanthanide coordination polymers with 3-pyridylpyrazole: Photophysical and magnetic properties. *Dalton Trans.* **2022**, *51*, 14673–14685. [[CrossRef](#)]
15. Ridenour, J.A.; Carter, K.P.; Butcher, R.J.; Cahill, C.L. RE-*p*-halobenzoic acid–terpyridine complexes, Part II: Structural diversity, supramolecular assembly, and luminescence properties in a series of *p*-bromobenzoic acid rare-earth hybrid materials. *CrystEngComm* **2017**, *19*, 1172–1189. [[CrossRef](#)]
16. Batrice, R.J.; Adcock, A.K.; Cantos, P.M.; Bertke, J.A.; Knope, K.E. Synthesis and characterization of an isomorphous lanthanide-thiophenemonocarboxylate series (Ln = La–Lu, except Pm) amenable to color tuning. *Cryst. Growth Des.* **2017**, *17*, 4603–4612. [[CrossRef](#)]
17. Kawamura, Y.; Wada, Y.; Hasegawa, Y.; Iwamuro, M.; Kitamura, T.; Yanagida, S. Observation of neodymium electroluminescence. *Appl. Phys. Lett.* **1999**, *74*, 3245–3247. [[CrossRef](#)]
18. Curry, R.; Gillin, W.P. 1.54  $\mu\text{m}$  electroluminescence from erbium (III) tris(8-hydroxyquinoline) (ErQ)-based organic light-emitting diodes. *Appl. Phys. Lett.* **1999**, *75*, 1380–1382. [[CrossRef](#)]
19. Mehrdel, B.; Nikbakht, A.; Aziz, A.A.; Jameel, M.S.; Dheyab, M.A.; Khaniabadi, P.M. Upconversion lanthanide nanomaterials: Basics introduction, synthesis approaches, mechanism and application in photodetector and photovoltaic devices. *Nanotechnology* **2021**, *33*, 082001. [[CrossRef](#)] [[PubMed](#)]
20. Fischer, S.; Ivaturi, A.; Fröhlich, B.; Rüdiger, M.; Richter, A.; Krämer, K.W.; Richards, B.S.; Goldschmidt, J.C. Upconverter silicon solar cell devices for efficient utilization of sub-band-gap photons under concentrated solar radiation. *IEEE J. Photovolt.* **2013**, *4*, 183–189. [[CrossRef](#)]
21. Bünzli, J.-C.G.; Eliseeva, S.V. Basics of lanthanide photophysics. In *Springer Series on Fluorescence: Lanthanide Luminescence: Photophysical, Analytical and Biological Aspects*; Wolfbeis, O.S., Hof, M., Eds.; Springer: Berlin/Heidelberg, Germany, 2011; Volume 7, pp. 1–46.
22. Davies, G.M.; Aarons, R.J.; Motson, G.R.; Jeffery, J.C.; Adams, H.; Faulkner, S.; Ward, M.D. Structural and near-IR photophysical studies on ternary lanthanide complexes containing poly (pyrazolyl) borate and 1,3-diketonate ligands. *Dalton Trans.* **2004**, *4*, 1136–1144. [[CrossRef](#)]
23. Bao, S.; Liang, Y.; Wang, L.; Wang, L.; Xu, L.; Wang, Y.; Liang, X.; Xiang, W. Superhigh-luminance Ce:YAG phosphor in glass and phosphor-in-glass film for laser lighting. *ACS Sustain. Chem. Eng.* **2022**, *10*, 8105–8114. [[CrossRef](#)]
24. Li, J.; Wang, L.; Zhao, Z.; Sun, B.; Zhan, G.; Liu, H.; Bian, Z.; Liu, Z. Highly efficient and air-stable Eu(II)-containing azacryptates ready for organic light-emitting diodes. *Nat. Commun.* **2020**, *11*, 5218–5225. [[CrossRef](#)] [[PubMed](#)]
25. Meyer, L.V.; Schönfeld, F.; Zurawski, A.; Mai, M.; Feldmann, C.; Müller-Buschbaum, K. A blue luminescent MOF as a rapid turn-off/turn-on detector for  $\text{H}_2\text{O}$ ,  $\text{O}_2$  and  $\text{CH}_2\text{Cl}_2$ , MeCN:  ${}^3_{\infty}[\text{Ce}(\text{Im})_3\text{ImH}]\cdot\text{ImH}$ . *Dalton Trans.* **2015**, *44*, 4070–4079. [[CrossRef](#)]
26. Matthes, P.R.; Müller-Buschbaum, K. Synthesis and characterization of the cerium(III) UV-emitting 2D-coordination polymer  ${}^2_{\infty}[\text{Ce}_2\text{Cl}_6(4,4'\text{-bipyridine})_4]\cdot\text{py}$ . *Z. Anorg. Allg. Chem.* **2014**, *640*, 2847–2851. [[CrossRef](#)]
27. Zhao, Z.; Wang, L.; Zhan, G.; Liu, Z.; Bian, Z.; Huang, C. Efficient rare earth cerium(III) complex with nanosecond *d–f* emission for blue organic light-emitting diodes. *Natl. Sci. Rev.* **2021**, *8*, nwa193. [[CrossRef](#)] [[PubMed](#)]
28. Frey, S.T.; Horrocks Jr., W.D. Complexation, luminescence, and energy transfer of  $\text{Ce}^{3+}$  with a series of multidentate amino phosphonic acids in aqueous solution. *Inorg. Chem.* **1991**, *30*, 1073–1079. [[CrossRef](#)]
29. Wang, Q.; Wu, W.; Zhang, J.; Zhu, G.; Cong, R. Formation, photoluminescence and ferromagnetic characterization of Ce doped AlN hierarchical nanostructures. *J. Alloys Compd.* **2019**, *775*, 498–502. [[CrossRef](#)]
30. Vadan, M.; Popovici, E.J.; Ungur, L.; Vasilescu, M.; Macarovici, D. Synthesis of luminescent strontium-magnesium orthophosphate activated with cerium and manganese. In Proceedings of the SIOEL'99: Sixth Symposium on Optoelectronics, Bucharest, Romania, 22–24 September 1999; pp. 111–116.
31. Youssef, H.; Sedykh, A.E.; Becker, J.; Taydakov, I.V.; Müller-Buschbaum, K. 3-(2-pyridyl)pyrazole based luminescent 1D-coordination polymers and polymorphic complexes of various lanthanide chlorides including orange-emitting cerium(III). *Inorganics* **2022**, *10*, 254. [[CrossRef](#)]
32. Youssef, H.; Becker, J.; Sedykh, A.E.; Schäfer, T.; Taydakov, I.V.; Müller-Buschbaum, K. Red emitting cerium(III) and versatile luminescence chromaticity of 1D-coordination polymers and heterobimetallic Ln/AE pyridylpyrazolate complexes. *Z. Anorg. Allg. Chem.* **2022**, *648*, e202200295. [[CrossRef](#)]

33. Youssef, H.; Sedykh, A.E.; Becker, J.; Schäfer, T.; Taydakov, I.V.; Li, H.R.; Müller-Buschbaum, K. Variable luminescence and chromaticity of homoleptic frameworks of the lanthanides together with pyridylpyrazolates. *Chem. Eur. J.* **2021**, *27*, 16634–16641. [CrossRef]
34. Shannon, R.D. Revised effective ionic radii and systematic studies of interatomic distances in halides and chalcogenides. *Acta Crystallogr. Sect. A Cryst. Phys. Diffr. Theor. Gen. Crystallogr.* **1976**, *32*, 751–767. [CrossRef]
35. Guo, Z.; Blair, V.L.; Deacon, G.B.; Junk, P.C. Europium is different: Solvent and ligand effects on oxidation state outcomes and C-F activation in reactions between europium metal and pentafluorophenylsilver. *Chem. Eur. J.* **2022**, *28*, e202103865. [CrossRef] [PubMed]
36. Drew, M.G.B.; Guillaneux, D.; Hudson, M.J.; Iveson, P.B.; Russell, M.L.; Madic, C. Lanthanide(III) complexes of a highly efficient actinide(III) extracting agent—2,6-bis(5,6-dipropyl-1,2,4-triazin-3-yl)pyridine. *Inorg. Chem. Commun.* **2001**, *4*, 12–15. [CrossRef]
37. O’Keeffe, M.; Peskov, M.A.; Ramsden, S.J.; Yaghi, O.M. The reticular chemistry structure resource (RCSR) database of, and symbols for, crystal nets. *Acc. Chem. Res.* **2008**, *41*, 1782–1789. [CrossRef]
38. Wells, A.F. *Three-Dimensional Nets and Polyhedra*; Wiley-Interscience: New York, NY, USA, 1977.
39. Guo, Z.; Luu, J.; Blair, V.; Deacon, G.B.; Junk, P.C. Replacing mercury: Syntheses of lanthanoid pyrazolates from free lanthanoid metals, pentafluorophenylsilver, and pyrazoles, aided by a facile synthesis of polyfluoroarylsilver compounds. *Eur. J. Inorg. Chem.* **2019**, *2019*, 1018–1029. [CrossRef]
40. Jiménez, J.R.; Díaz-Ortega, I.F.; Ruiz, E.; Aravena, D.; Pope, S.J.A.; Colacio, E.; Herrera, J.M. Lanthanide tetrazolate complexes combining single-molecule magnet and luminescence properties: The effect of the replacement of tetrazolate N<sub>3</sub> by  $\beta$ -diketonate ligands on the anisotropy energy barrier. *Chem. Eur. J.* **2016**, *22*, 14548–14559. [CrossRef]
41. Hughes, I.D.; Däne, M.; Ernst, A.; Hergert, W.; Lüders, M.; Poulter, J.; Staunton, J.B.; Svane, A.; Szotek, Z.; Temmerman, W.M. Lanthanide contraction and magnetism in the heavy rare earth elements. *Nature* **2007**, *446*, 650–653. [CrossRef]
42. Carnall, W.T.; Fields, P.R.; Rajnak, K. Electronic energy levels of the trivalent lanthanide aquo ions. IV. Eu<sup>3+</sup>. *J. Chem. Phys.* **1968**, *49*, 4450–4455. [CrossRef]
43. Carnall, W.T.; Fields, P.R.; Rajnak, K. Electronic energy levels of the trivalent lanthanide aquo ions. III. Tb<sup>3+</sup>. *J. Chem. Phys.* **1968**, *49*, 4447–4449. [CrossRef]
44. Seidel, C.; Lorbeer, C.; Cybińska, J.; Mudring, A.-V.; Ruschewitz, U. Lanthanide coordination polymers with tetrafluoroterephthalate as a bridging ligand: Thermal and optical properties. *Inorg. Chem.* **2012**, *51*, 4679–4688. [CrossRef]
45. Huskowska, E.; Turowska-Tyrk, I.; Legendziewicz, J.; Riehl, J.P. The structure and spectroscopy of lanthanide(III) complexes with 2,2'-bipyridine-1,1'-dioxide in solution and in the solid state: Effects of ionic size and solvent on photophysics, ligand structure and coordination. *New J. Chem.* **2002**, *26*, 1461–1467. [CrossRef]
46. Fernández-Fernández, M.d.C.; Bastida, R.; Macías, A.; Pérez-Lourido, P.; Platas-Iglesias, C.; Valencia, L. Lanthanide(III) complexes with a tetrapyrroline pendant-armed macrocyclic ligand: <sup>1</sup>H NMR structural determination in solution, X-ray diffraction, and density-functional theory calculations. *Inorg. Chem.* **2006**, *45*, 4484–4496. [CrossRef] [PubMed]
47. Bochkarev, M.N.; Khoroshenkov, G.V.; Schumann, H.; Dechert, S. A novel bis(imino)amine ligand as a result of acetonitrile coupling with the diiodides of Dy(II) and Tm(II). *J. Am. Chem. Soc.* **2003**, *125*, 2894–2895. [CrossRef]
48. Sedykh, A.E.; Kurth, D.G.; Müller-Buschbaum, K. Two series of lanthanide coordination polymers and complexes with 4'-phenylterpyridine and their luminescence properties. *Eur. J. Inorg. Chem.* **2019**, *2019*, 4564–4571. [CrossRef]
49. Matthes, P.R.; Eyley, J.; Klein, J.H.; Kuzmanoski, A.; Lambert, C.; Feldmann, C.; Müller-Buschbaum, K. Photoluminescent one-dimensional coordination polymers from suitable pyridine antenna and LnCl<sub>3</sub> for visible and near-IR emission. *Eur. J. Inorg. Chem.* **2015**, *2015*, 826–836. [CrossRef]
50. Bünzli, J.-C.G.; Comby, S.; Chauvin, A.-S.; Vandevyver, C.D.B. New Opportunities for Lanthanide Luminescence. *J. Rare Earths* **2007**, *25*, 257–274. [CrossRef]
51. Dexter, D.L. A theory of sensitized luminescence in solids. *J. Chem. Phys.* **1953**, *21*, 836–850. [CrossRef]
52. Dang, S.; Yu, J.; Wang, X.; Sun, L.; Deng, R.; Feng, J.; Fan, W.; Zhang, H. NIR-luminescence from ternary lanthanide [Ho<sup>III</sup>, Pr<sup>III</sup> and Tm<sup>III</sup>] complexes with 1-(2-naphthyl)-4,4,4-trifluoro-1,3-butanedionate. *J. Lumin.* **2011**, *131*, 1857–1863. [CrossRef]
53. Kahn, O. *Molecular Magnetism*; Wiley-VCH: Weinheim, Germany, 1993.
54. Pham, Y.H.; Trush, V.A.; Carneiro Neto, A.N.; Korabik, M.; Sokolnicki, J.; Weselski, M.; Malta, O.L.; Amirkhanov, V.M.; Gawryszewska, P. Lanthanide complexes with N-phosphorylated carboxamide as UV converters with excellent emission quantum yield and single-ion magnet behavior. *J. Mater. Chem. C* **2020**, *8*, 9993–10009. [CrossRef]
55. Benelli, C.; Gatteschi, D. Magnetism of lanthanides in molecular materials with transition-metal ions and organic radicals. *Chem. Rev.* **2002**, *102*, 2369–2388. [CrossRef] [PubMed]
56. Del Giudice, M.R.; Mustazza, C.; Borioni, A.; Gatta, F.; Tayebati, K.; Amenta, F.; Tucci, P.; Pieretti, S. Synthesis of 1-methyl-5-(pyrazol-3-yl)- and 1,2,4-triazol-3- and 5-yl)-1,2,3,6-tetrahydropyridine derivatives and their evaluation as muscarinic receptor ligands. *Arch. Pharm. Pharm. Med. Chem.* **2003**, *336*, 143–154. [CrossRef] [PubMed]
57. Bauer, V.J.; Dalalian, H.P.; Fanshawe, W.J.; Safir, S.R.; Tocus, E.C.; Boshart, C.R. 4-[3(5)-Pyrazolyl]pyridinium salts. A new class of hypoglycemic agents. *J. Med. Chem.* **1968**, *11*, 981–984. [CrossRef] [PubMed]
58. Sheldrick, G.M. SHELXT—Integrated space-group and crystal-structure determination. *Acta Crystallogr. Sect. A Found. Crystallogr.* **2015**, *71*, 3–8. [CrossRef] [PubMed]
59. Sheldrick, G.M. Crystal structure refinement with SHELXL. *Acta Crystallogr. Sect. C Struct. Chem.* **2015**, *71*, 3–8. [CrossRef]

60. Spek, A.L. PLATON SQUEEZE: A tool for the calculation of the disordered solvent contribution to the calculated structure factors. *Acta Crystallogr. Sect. C Struct. Chem.* **2015**, *71*, 9–18. [[CrossRef](#)]
61. Spek, A.L. Structure validation in chemical crystallography. *Acta Crystallogr. Sect. D Biol. Crystallogr.* **2009**, *65*, 148–155. [[CrossRef](#)]
62. Spek, A.L. What makes a crystal structure report valid? *Inorg. Chim. Acta* **2018**, *470*, 232–237. [[CrossRef](#)]
63. Spek, A.L. CheckCIF validation ALERTS: What they mean and how to respond. *Acta Crystallogr. Sect. E Crystallogr. Commun.* **2020**, *76*, 1–11. [[CrossRef](#)]
64. Spek, A.L. Single-crystal structure validation with the program PLATON. *J. Appl. Crystallogr.* **2003**, *36*, 7–13. [[CrossRef](#)]
65. Blatov, V.A.; Shevchenko, A.P.; Proserpio, D.M. Applied topological analysis of crystal structures with the program package topospro. *Cryst. Growth Des.* **2014**, *14*, 3576–3586. [[CrossRef](#)]
66. Pennington, W.T. DIAMOND—Visual crystal structure information system. *J. Appl. Crystallogr.* **1999**, *32*, 1028–1029. [[CrossRef](#)]
67. Coelho, A.A. TOPAS and TOPAS-Academic: An optimization program integrating computer algebra and crystallographic objects written in C++. *J. Appl. Crystallogr.* **2018**, *51*, 210–218. [[CrossRef](#)]

**Disclaimer/Publisher’s Note:** The statements, opinions and data contained in all publications are solely those of the individual author(s) and contributor(s) and not of MDPI and/or the editor(s). MDPI and/or the editor(s) disclaim responsibility for any injury to people or property resulting from any ideas, methods, instructions or products referred to in the content.